Sensory dependencies rapidly and autonomously yield generalizable representations in recurrent cortical-like networks

Udaya B. Rongala[1] and Henrik Jörntell[1]

[1] *Neural Basis of Sensorimotor Control, Department of Experimental Medical Science, Lund University, Lund, Sweden*

correspondence e-mail: udaya_bhaskar.rongala@med.lu.se, henrik.jorntell@med.lu.se

Abstract

How do biological brains become operational so quickly? Here we introduce a 'neuromorphic' learning strategy that mimics the strategies of animals in early development. It consists of continual random activations of the body, which is a mechanically coupled system with rich, dynamic intrinsic sensor dependencies. Using a dynamic model of biological skin tissue with distributed sensors, we trained small, recurrent networks designed to emulate a primordial cortex with excitatory and inhibitory neurons and simultaneous independent learning in both types of synapses. Continual random activations of the skin, without resetting the network state, led to rapid acquisition of remarkably generalizable representations with emergent predictive capability. The network could separate inputs and solve a kinematics task it had never encountered, even when substantial parts of the sensor population were removed. This strategy of learning the dominant regularities in dynamic sensory information can explain efficient learning of complex operation in the brain.

A striking difference between biology and artificial intelligence network technology is that biological neuronal networks seem to be learning effectively from much fewer examples and much less repetitious inputs (1). We hypothesized that one reason could be that the brain learns about the world through the biomechanical constraints and enablers provided by its body. The body is composed of tissues with dynamic compliances, such as in the skin (2) but also in deep tissues in general, which essentially make the whole body mechanically coupled (3). Because the biological sensors are embedded within such tissues, they can display complex patterns of dynamic dependencies, translating to spatiotemporal regularities in their population level activity (2). Combining such regularities could be used to represent in principle any conceivable complex, distributed stimulus by means of the principle of superposition (2, 4, 5, 6). A learning strategy that focuses on such regularities, through varied rather than repetitious behavior, could therefore rapidly result in more efficient and generalizable network representations, and could be more robust to sensor loss and/or sensor drift.

We tested the general principles of this postulate by studying learning from sensor inputs generated by a recent model of skin tissue dynamics (2) in a recurrent neuronal network, which was made as small and generic as possible while still being a relevant comparison to simplified subnetworks of primordial cortex (7, 8). The two-layered network was composed of fully connected excitatory and inhibitory neurons (Fig. 1A) where each excitatory and inhibitory synapse was independently and continuously subject to Hebbian-like plasticity. We used a non-spiking

neuron model (8), which emulates the impact of membrane time constants and conductance-based synaptic integration in biological neurons. The skin sensory inputs were provided to the first layer, to both excitatory and inhibitory neurons, although without a thalamus. Our fully connected network was motivated by that recurrent excitatory loops are a common feature in neocortical circuits (9, 10, 11, 12, 13, 14, 15), that inhibitory interneurons provide lateral inhibition (16, 17, 18, 6) as well as feed-forward inhibition (19, 20), but also make synapses on other inhibitory neurons, thereby also potentially forming recurrent disinhibitory loops (21, 22, 23, 24). Hence, both excitatory and inhibitory synapses can form all-to-all local cortical networks (15) in addition to providing long range intracortical connections (25, 26, 27). Both neuron types receive both local and long range intracortical connections as well as thalamic sensory inputs (19, 28).

Results

Network learning from intrinsic dependencies

Figure 1B illustrates the mass-spring-damper implementation of the dynamic skin model (2) used to model skin tissue dynamics. Although the skin model could provide 1000's of sensor signals we used only 10 of those sensors, which corresponded to the force signals generated in the 10 springs connected to the central mass (indicated in black in Figure 1B). Figure 1C shows one example of skin sensor activation to a given skin input (top panel). The temporal profiles of the sensor responses illustrate that each sensor provided non-redundant information, despite their mechanical dependencies. When the other four types of skin inputs were also considered, the relative uniqueness of the signal of each individual sensor was even more clear (Fig. S1).

As the actions driving early learning in biological brains are far from structured ('*motor babbling*'; see (29, 30)), our network learning consisted of a series of random, non-repetitive activations of the skin model (1160 stimulus presentations), in what would correspond to less than one hour of random haptic interaction in a biological system. The continual nature of the activations also meant that the circulating activity within the recurrent network was never allowed to fully relax between consecutive stimuli. Hence, each stimulus presentation was met with a potentially unique processing state in the network, rendering each learning phase even more unique. To test the impact of the intrinsic dependencies across the sensor population, we compared the network learning from the skin inputs ('skin network') with the same network instead learning from pre-generated random patterns of Gaussian signals ('Gaussian network') (Fig 1C). We generated Gaussian signals to match the overall frequency and power distribution of the skin inputs (Fig S2). Figure 1D-G illustrates the neuron activities comprehensively as well as in detailed snapshots, pre- and post-learning, for the 'skin network' as well as for the 'Gaussian network'. The neuron signals became more diversified in the skin network compared to the Gaussian network (Fig. 1F,G), i.e. there was a richer set of covariance patterns across the neuron population.

Separation of naive inputs

Our critical research question was if the skin network could separate inputs that it had not previously experienced. To address this question, we analyzed the activity distribution patterns across the neuron population using principal component analysis (PCA) (i.e. quantifying any regularities in the network activity arising as a consequence of learning). Post-learning skin networks and Gaussian networks (Fig. 2A) were provided skin inputs they had not ex-

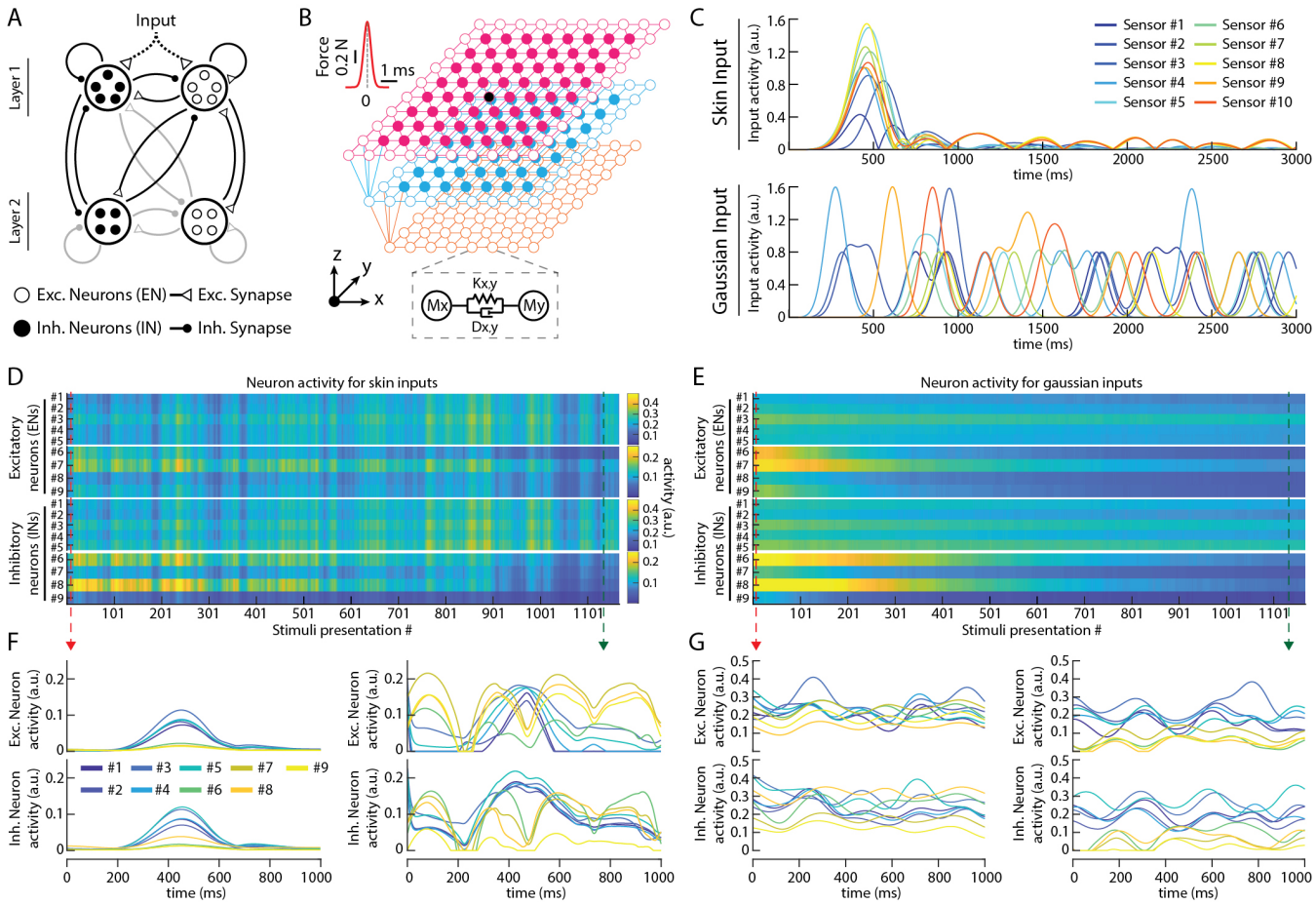

Figure 1: **Learning from sensors embedded in a dynamic skin tissue model** (**A**) Schematic of the fully connected network structure. (**B**) Three-layer damped mass-spring skin model (2) used to generate the intrinsically dependent sensory inputs. Top left corner, time profile of the applied forces for the different inputs. Masses, shown as nodes, were connected by springs and dampers represented as links (internode distance 1.0 mm). Note that the actual model was larger and comprised 1085 nodes in total. Nodes shown as circles along the edges were fixed nodes, including the entire third layer. The activity from the 10 sensors connecting to the mass at the center of the superficial layer (black node) were provided as input to the network. (**C**) Example sensory input used for network learning. *Top:* Skin model sensor inputs; *Bottom* Gaussian sensor inputs. (**D**) Individual neuron activities (moving average across 50 input presentations) during learning from an uninterrupted sequence of 1160 random skin inputs. This network had initial connectivity%=23. (**E**) Corresponding network learning from the Gaussian inputs. (**F**) Activities of the excitatory (top) and inhibitory (bottom) neurons (N=9 neurons per group, blue neurons were located in layer 1) to an example skin input at the beginning (left) and at the end (right) of the learning. (**G**) Similar display for a Gaussian input.

perienced during the training (Fig. 2B). These inputs differed either with respect to their spatial force input patterns (Fig. S1) or they consisted of different temporal profiles/kinematics of non-patterned force impulses (Fig. S3). We also tested the impact of removing sensors (Fig. 2B) post-learning. For the five naive spatial skin inputs, the skin networks provided more distinctly different neuron population activity trajectories in the PC space than the Gaussian networks (Fig. 2C); Fig. S4 illustrates the PC trajectories for the untrained initial random network), and also provided better classification accuracy across different neuronal noise levels (Fig. 2D). Notably, when removing 20% of the sensors, the PC trajectories did not substantially alter (Fig. S5) and the classification was unchanged or improved for the skin network, in contrast to the Gaussian network (Fig. 2D, bottom panel). We next tested the performance of the networks for a task where an identical spatial force distribution was repeated but with different durations and speeds of the change in force (Fig. S3), i.e. here the task was instead to separate inputs with different kinematic properties. For the separation of force impulses with different kinematics, which was hence a type of

task that the networks had not been trained on, there was an even clearer separation between the two network types (Fig. 2E,F), even more so with sensor loss (Fig. 2F, bottom panel). Across all tests, the skin network, unlike the Gaussian network, outperformed the pre-learning network, except at the lowest noise levels where the networks approached deterministic behavior. The fact that even the untrained network could separate inputs during deterministic operation is in line with that Reservoir Computing networks, used in the field of AI, normally have intrinsic dynamic modes without any training in the network, which can provide some level of separation capacity for dynamic inputs (31). However, normally neurons in the brain *in vivo* do not operate without noise (32, 33) and hence we believe our higher noise levels are more reflective of what the brain can achieve in terms of input separation. Hence, learning on inputs with intrinsic consistencies in its dynamics, regardless of the type of activation used to drive those inputs, led to an improvement in the generalized separation capacity of the network, whereas training on dynamic inputs without such intrinsic consistencies could even lead to a performance loss compared to the randomly connected pre-learning network.

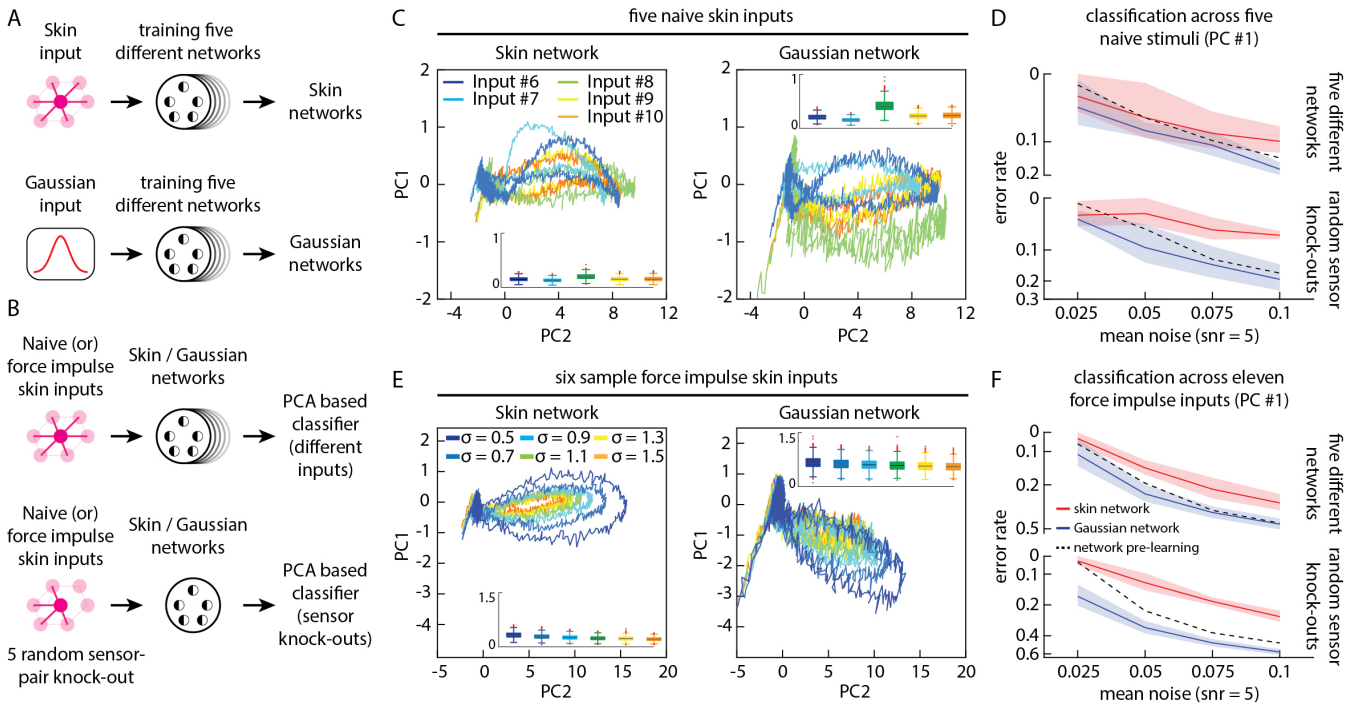

Figure 2: **Generalization to naive inputs and robustness to sensor loss in skin networks** (**A**) The network learned from skin inputs or from Gaussian inputs. (**B**) Protocols used for comparing the classification generalization and robustness. (**C**) The responses of the excitatory neuron population for the five naive skin inputs Fig. S1 F-J; color coded) projected on the first two principal components (PCs), comparing the skin and Gaussian networks (at a neuronal noise level of 0.1). *Inset*: the variances of the PC scores for the five different inputs. Same network as in Fig. 1. (**D**) Classification accuracies (mean and variance) across the five naive skin inputs at different noise levels. (**bottom**) Classification accuracies across the same five naive skin inputs with random sensory knock-out. (**E**) Similar display as in **C**, but for eleven force impulse skin inputs (Fig. S3). (**F**) Classification accuracy across these eleven force impulse skin inputs.

Synaptic weight changes

Relative to the untrained network (Fig. 3A-C), skin inputs caused an increase in the weights of the sensory synapses, whereas the opposite effect applied to the Gaussian network (Fig. 3D; note the scale difference for the two networks). There were also extensive reorganization and excitatory/inhibitory re-balancing of the internal network synapses (Fig. 3E, Fig. S6, S7), which can explain how the skin network activity could decrease (Fig. 1D,E) as its synaptic

weights increased. We repeated the same learning for 30 different network settings, each fully connected, identified by their 'Initial connectivity%'. This label was reflective of the mean weights of the synapses (the initial network activities scaled roughly linearly with the 'Initial connectivity%'s (Fig. S11)) but also an index indicating the weight distribution (see Fig. S8, S9) and skewness (Fig. S10), in order to test our learning strategy for a wide range of initial network connectivity distributions. As illustrated in Fig. 3F-I, the synaptic weight changes in the two types of neurons (excitatory and inhibitory) were approximately congruent across the different Initial connectivity%'s for the two network types (skin and Gaussian). Whereas the sensory synapses changed the most, the internal network synapses could change almost as much for the networks with intermediate Initial connectivity% (20-35%), in particular the feedback connections from layer 2 to layer 1 (Fig. S12). We also tested if the initial weight skewness could explain these weight changes more clearly, but found no apparent relationship (Fig. S13). Notably, the skin networks with the highest Initial connectivity (%) did not display much weight changes (Fig. 3F-I) and as we found out next this greatly impacted the separation of the inputs.

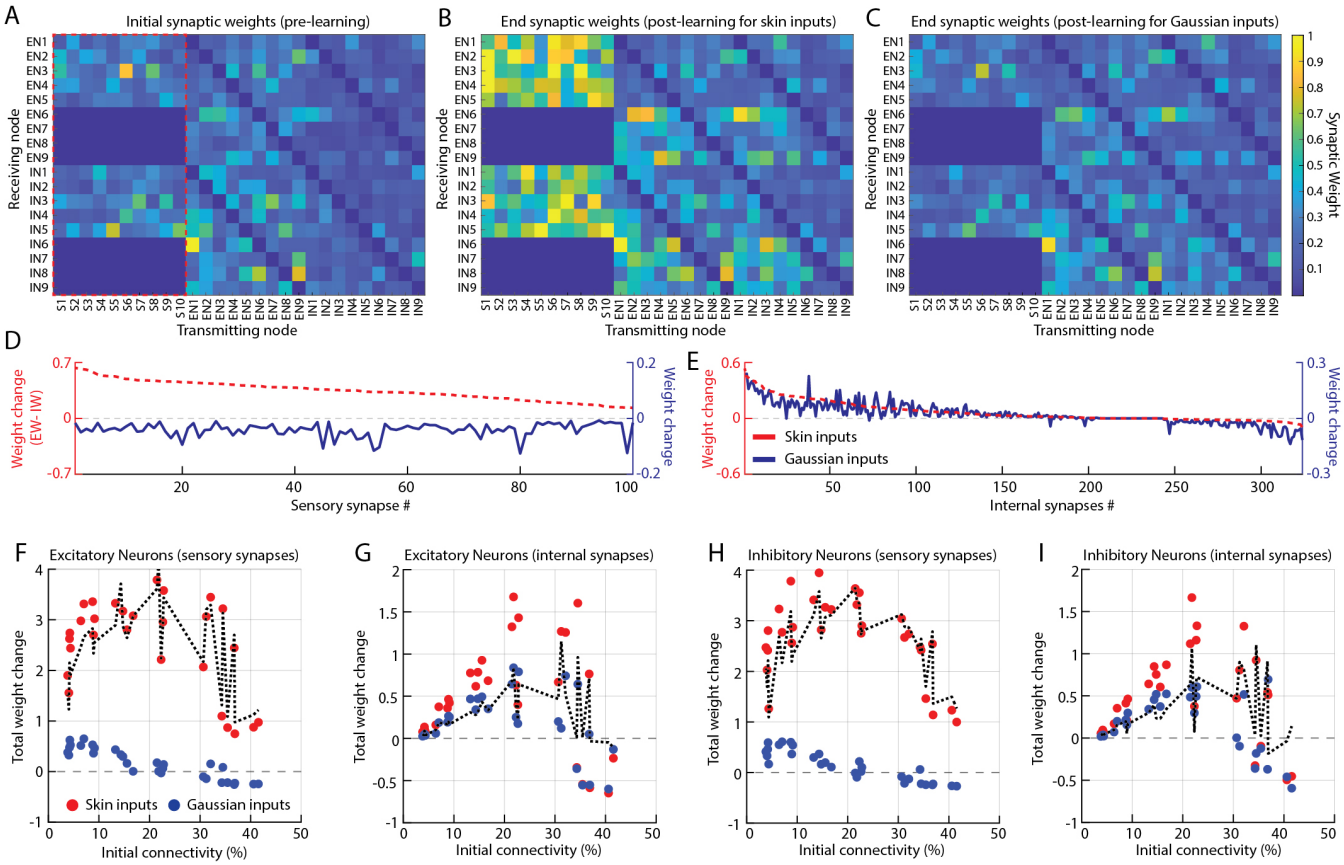

Figure 3: **Synaptic weight changes following learning** (**A**) Initial synaptic weights for an example network with the sensory synapses within the red dotted box. (**B**) The synaptic weights post-learning (end Weights) in the skin network. (**C**) The synaptic weights post-learning in the Gaussian network. (**D**) Sensory synapses sorted by their magnitude of weight change after learning from the skin input, for comparison of the skin network and the corresponding Gaussian network. (**E**) Similar display as in **D**, but for weight changes across non-sensory synapses (internal synapses). (**F-I**) Average net weight changes post-learning, sorted by type of synapse, across networks with varied initial weight configuration (Fig. S8, S9). The dashed lines indicate the difference in average net weight changes between the corresponding skin networks and the Gaussian networks.

The importance of differentiation of the activity distribution across the neurons

The quantification of the input separation in Fig. 2 depended on the time series of activity distribution patterns across the neuron population. Differentiations of the activity distributions across different inputs, indicative of a complementarity of the neuronal encoding, can be viewed as a proxy for the input separation capability of the network (5, 34, 35) and cortical neuron populations display a great degree of differentiation in their activity patterns across various input conditions (34, 36, 37, 38, 39). The reason why this is so can be sought from studies of recurrent variational autoencoders, a type of artificial neural network, where the enforcement of such differentiation between the neural nodes during the learning of a dynamics tasks leads to more efficient representations (40).

When we quantified the complementarity of the neuronal encoding we did indeed observe that the cross-correlation measure between the neurons decreased substantially with learning in the skin networks (Fig. 4A,B). However, for the networks with the highest connectivity% such a drop did not occur. These networks also had the lowest degree of restructuring of their synaptic weights (Fig. 3F-I) and it appeared that the intrinsic dynamics in these tight networks were too strong to become sufficiently impacted by the sensory synaptic activities. We investigated if a drop in the cross-correlation in these cases could be 'rescued' by a tweak to the learning rule, which relied on the activity correlation between the synapse and the postsynaptic signal. In this tweak, the excitatory synapses were only allowed to 'see' a high pass filtered version of the postsynaptic signal for its learning (See Methods for the biological rationale). Implementing this 'Excitatory synapse learning signal filter' led to drops in the cross-correlations for networks with high initial connectivity%, with almost no impact on networks with the lowest initial connectivity% (Fig. 4C, Fig. S15). Also the overall pattern of synaptic weight changes remained unchanged (compare Fig. S16 with Fig. 3F-I). Importantly, for the networks with high initial connectivity%, the learning signal filter did indeed also lead to a 'rescue' of their input separation capability (Fig. 4D; the filter improved the classification error rate (cf. Fig. 2D,F) from 0.12 (left) to 0.01 (right)). Simultaneous excitatory and inhibitory synaptic plasticity, where both synapse types used the same learning rule, should in principle lead to the inhibition cancelling out the excitation in the network. However, as the sensory input is excitatory, inhibition will always be lagging 'one step behind', leaving some net excitation and this incomplete inhibition will lead to decorrelation between the neurons (Fig. 5). In the networks with lower connectivity%, the initial synaptic weight discrepancies between the neurons is higher so it should be harder for inhibition to catch up with the excitatory pathways within the network that happened to be provided already in the random seed weights. In the networks with higher connectivity%, in contrast, such inhibitory-excitatory synaptic weight mismatches are not provided 'for free' to the same extent. The excitatory learning signal filter helps creating such pathways, and could in this way cause a differentiation in the activities between the neurons across the network, which was necessary to achieve a better input separation also in the tightly connected networks. At the cellular mechanistic level, the learning signal filter could be achieved for example by that the dendritic spines, which only receive excitatory synapses (41), modify the signal available to the postsynaptic enzymatic machinery that controls the synaptic weights within each synapse (6). An actual measurement of the biological fine tuning of the excitatory and inhibitory synaptic plasticity rules in this regard *in vivo*, would require far greater precision than what can currently be provided experimentally.

Finally, removing inhibitory synapses, both laterally within the layers and feed-forward connections, led to significantly higher cross-correlations (Fig. S17) and these connections would hence be particularly important to support a high separation capacity.

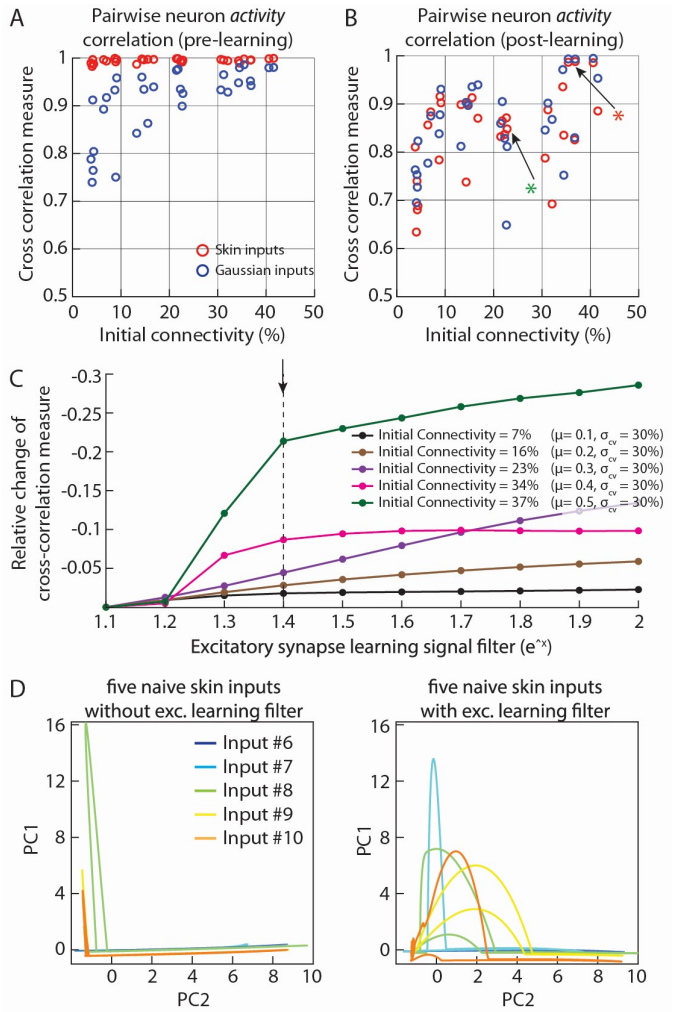

Figure 4: **Diversification of the neuronal activity post-learning and 'rescue' effect of the excitatory learning signal filter.**(**A**) Average pairwise cross-correlations across all the ENs pre-learning. (**B**) Same observation post-learning. Arrow with *green asterisk* indicate the network illustrated in Figs 1, 2 and the arrow with *red asterisk* indicate the network that failed to learn without learning signal filter. (**C**) Relative changes in the cross correlation measure in skin networks across different learning signal filter exponents. Dashed line indicates the exponent (1.4) used in the test in (D). (**D**) PC trajectories of the failing post-learning network without the learning signal filter (left) and the same network with the learning signal filter (right).

Discussion

The main point of the present paper was to illustrate the impact of a neuromorphic learning strategy, which depended on inputs from sensors distributed across a system with rich internal mechanical couplings and dynamics, similar to biological skin tissue, in a recurrent, cortex-style neuronal network. Learning was achieved using diverse spatiotemporal inputs to the tissue, compatible with early biological development, which is characterized by mostly disorganized, semi-chaotic movements (42, 29, 43, 44). The learning was independently controlled by each individual excitatory and inhibitory synapse, and hence the identification of the regularities in the sensory inputs were achieved fully autonomously by the network. We found this neuromorphic learning strategy to quickly converge to highly generalizable network representations, applicable to separate inputs that differed in their spatial and/or kinematic character compared to those experienced during network learning, and to make the acquired representations robust to sensor loss.

With the neuromorphic learning strategy we argue that the most important aspects of the sensory information

for the brain would be which dependency states that apply across the sensor population (5), i.e. the regularities, or the invariants, in the spatiotemporal patterns of the sensor population activity. In this representation strategy, the details of individual sensor activation patterns become less relevant, which we showed with the conserved separation capacity when 20% of sensors were removed post-learning (Fig. 2). Since the regularities across the sensors derive from the mechanical couplings in the tissue, they will reappear across in principle any stimulus/activation context and can thus be used by the network to separate stimuli that are dissimilar from those previously experienced. The aspects of the sensor population regularities that are the most in concert with the intrinsic network dynamics will also be the most easily learnt by the network, which consequentially will gradually become better at mirroring the dominant mechanical dynamics of the tissue (i.e. its regularities). This was indicated by that the learning created attractor-like temporal trajectories in the activity distributions across the neuron population (Fig. 2). Interestingly, when the network begins to mirror the dominant dynamics in the mechanical system, this is equivalent to that the network begins to predict its properties. Our network architecture and learning mechanisms therefore feature specific low-level network mechanisms that can achieve predictive coding, which is widely held to be an important mode of operation in the cortex (45, 46, 47) but not previously shown how it could arise as an emergent, rather than imposed by design, network property.

We studied the plasticity-driven emerging functional roles for synaptic inhibition and synaptic excitation when there was no *a priori* constraint on their connectivity or learning. The neurocomputation literature instead often isolates excitatory from inhibitory synaptic plasticity during the learning process or considers inhibitory synapse learning as a homeostatic reaction to the learning in the excitatory synapses (48, 49, 50, 51, 52, 53). It is common practice to regard the inhibition as having a specific role, such as feed-forward, feedback or blanket inhibition. More selective inhibition has also been modeled (54), in which case it could contribute to subsets of neurons conducting more independent computations (55, 56, 57, 58). But in recurrent networks, it is hard to see how functionally 'clean' roles of inhibition could exist (Fig. 5A). A ground truth here could be that the division into excitatory and inhibitory neurons leads to that the inhibition can act to subtract aspects of the information (sensory or network-internal) that the network already 'knows' hence leaving 'unknown' information to be processed by other neurons in the network (Fig. 5B), both at the 'global' and at a more 'detailed' level, to use a proposed terminology (48). The neuromorphic learning strategy presented here supports emerging, self-organizing predictive coding in cortical-like, recursive networks. Future studies can use this as a framework to study the operation of cortical networks *in vivo* more integratively. Future studies could also establish appropriate benchmarks to more systematically demonstrate the performance of neuromorphic learning networks, not the least in tasks requiring predictions.

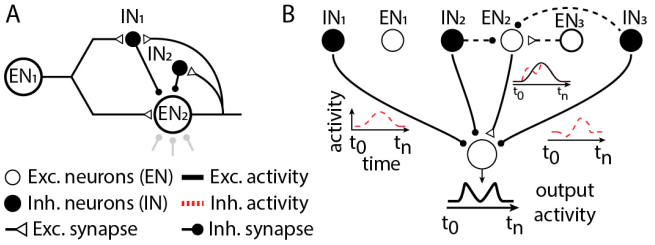

Figure 5: **Functional roles of parallel synaptic inhibition and excitation.**(**A**) Scenario when feed-forward inhibition and feedback inhibition are mediated by the same inhibitory interneuron. If multiple inhibitory interneurons provide input to EN_2 (shaded synapses below EN_2), the inhibitory control can sometimes have the properties of 'Detailed' inhibition, and sometimes have the property of 'blanket' or 'global' inhibition (see text). (**B**) A feed-forward excitatory pathway via EN_2 would lose its signal if the inhibitory signal is identical. A more diversified inhibition can help rescuing parts of the excitatory signal propagation through signal derivation.

Materials and Methods

Network Connectivity

We simulated two-layer fully connected recursive neuronal networks comprising both excitatory neurons (ENs) and inhibitory neurons (INs) (Fig. 1A). There were five ENs & five INs in layer 1 and four ENs & four INs in layer 2. Only the ENs and INs in layer 1 received external sensory inputs (see section *Sensory Inputs*) as excitatory synaptic connections. We did not examine autapses (self-excitatory/inhibitory connections) as they were previously observed to amplify the high-frequency parasitic oscillations within recurrent networks with these neuron specifications (8).

Neuron Model

Our previously published non-spiking linear summation neuron model (LSM) was used to compute the activity of both excitatory and inhibitory neurons. LSM is a compact model capturing the central characteristics of an H-H conductance-based neuron model (8) where the time-continuous output activity is intended to reflect the mean firing rate of a traditional spiking neuron model. In LSM, the membrane potential (A, Eq. 1) of a neuron is given by the summation of weighted (w) input synaptic activity (a), that is normalized by emulated membrane conductances (static leak and dynamic leak). The static leak (k) emulates the leak channels contributing to the resting membrane potential and is scaled by the total number of synaptic inputs (i) to the given neuron ($k = 0.25$ per synapse). The dynamic leak (τ) reflects the rate of leak towards the resting potential, normally limited by the membrane capacitance of the neuron, which was a constant ($\tau = 1/100$). The scaling effects of these membrane constants on the neuron activity under various synaptic input conditions were previously reported in (8). The neuron output activity was thresholded at a membrane potential corresponding to zero net synaptic input activity in the neuron (Eq. 2). The neuron activity of LSM is given by Eq. 1 & 2.

$$\tau \frac{dA}{dt} = \frac{\sum(w_i.a_i)}{k + \sum |w_i.a_i|} \tag{1}$$

$$if A < 0, then A = 0 \tag{2}$$

Sensory Inputs

Skin Model

A on mass-spring-damper model of a slab of skin (Fig. 1B) was used to generate the sensory input signals (*skin inputs*). This skin model was previously developed to replicate the dispersive mechanical waves that are elicited in biological skin during tactile interaction (2). The spreading mechanical waves, also studied in other experiments (59, 60, 61) create differential skin tissue movements, similar to shear forces (62), that are known to activate the skin mechanosensors, and that create extraordinary rich skin sensor information (2). The masses (circles, Fig. 1B) in this skin model were arranged in three layers superficially resembling the structural properties of human skin (epidermis, dermis and subcutaneous tissues). The masses were homogeneously distributed in a mesh-grid-like structure along each layer, and in pyramidal structures across layers (color coded as per layer, Fig. 1B). The neighbouring masses were interconnected via a network of springs and dampers (lines, Fig. 1B). In this study the skin model has a mesh

size of 20×20 masses in layer 1 (400 masses), 19×19 masses in layer 2 (361 masses) and 18×18 masses in layer 3 (324 masses); interconnected with a 5770 springs and dampers. The model uses the inter-node distance, which is a representation of strain, corresponding to the spring load, as the best available proxy for representing the signal that would drive the activation of mechanoreceptors. The masses on the edges of the skin model (empty circles, Fig. 1B) were fixed in all three axes. To compute the numerical integration, the equation of motion (Eq. 3) for multiple degree-of-freedom spring-mass-damper system can be written in state-space form as in equation 4 (63, 2)

$$M\ddot{q} + C\dot{q} + Kq = f \tag{3}$$

Where M, C and K are matrices denoting mass, stiffness and damping of the whole system and f is the input force vector. q, $\dot{q}$ and $\ddot{q}$ are denoting position, velocity and acceleration of the system respectively.

$$\dot{x}(t) = Ax(t) + Bu(t) \tag{4}$$

Where x is the state vector, u is the applied input force, A is the state matrix, and B is the input matrix. Coupling equation 3 and 4, we obtain

$$M\ddot{q}(t) = -C\dot{q}(t) - Kq(t) + f(t) \tag{5}$$

Which can be written as,

$$\ddot{q}(t) = \begin{bmatrix} 0 & I \\ -M^{-1}K & -M^{-1}C \end{bmatrix} x(t) + \begin{bmatrix} 0 \\ M^{-1} \end{bmatrix} f(t) \tag{6}$$

To compute the numerical solution of the above-described state equation we used an *ode45* solver (fifth order Runge-Kutta method) in MATLAB, with a time step of 0.01 ms. Each mass within the skin model moved freely in the three-dimensional space, the matrices and vectors in the above defined state equation were adapted accordingly. The values of $M, K\&C$ are $1.0\,\mathrm{mg},\ 2.5\,\mathrm{N\,m^{-1}}$ & 5x$10^{-4}\mathrm{N\,s\,m^{-1}}$, as studied in (2).

Skin Inputs

To activate the skin sensors, we designed different spatial skin force patterns that were activated by defining the input force vector (f) of equation 6 as a Gaussian function with a sigma of $1ms$ (Fig 1B, insert). The force vector was three dimensional ($f = [f_x f_y f_z]$), describing the input force across all three axis of the skin. The obtained force across each spring was used as the as the output signals of the skin model, used to drive the activity of the neuronal network (*Skin Input*, Fig. 1C). The forces were given by Hooke's law ($F_s = kx$), where k is the stiffness constant of the spring and x is the rate of change in the position from equilibrium. Out of the 5770 springs available in this skin model, we use only the ten springs connected to the mass in the center of layer 1 (black mass, Fig. 1B). The responses of these ten springs were used for training and testing the networks.

Gaussian Input

As a comparison for the networks that learned from skin model inputs, which have systematic intrinsic dependencies or sensor population regularities across all inputs, we also let some networks learn from 'Gaussian inputs' that lacked such intrinsic dependencies. For each of the 10 Gaussian 'sensors', we used pseudo-random spike trains

with a spiking frequency of 1-3 Hz frequency drawn from a normal distribution and convoluted using a Gaussian function to obtain a time-continuous sensory input (*Gaussian Input*, Fig. 1C). An inbuilt MATLAB function "*randi*" was used to generate the spike time distributions and "*gaussmf*" was used for the convolution of the spikes into time-continuous responses. The distribution and convolution parameters for generating the Gaussian activity were chosen to match the power and frequency components of the skin inputs (Fig. S2).

Network Training

For learning we provided the network (Fig. 1A) with a series of 1160 stimulus presentations, either sensory inputs from the skin model or from the Gaussian model (Fig. 1C). A network that learnt from the skin inputs is referred as "*skin network*" and a network that learnt from the Gaussian inputs is referred as "*Gaussian network*". For the skin networks, we used 50 unique skin activation conditions, consisting of five different activations (*indent, push, pull, slide, point push,* Fig. S1) at ten different locations on the surface of the skin model, provided in a predefined (pseudo-)random order. For the Gaussian networks, we generated non-repetitive random activity patterns across the 10 sensors. For both skin and Gaussian training inputs, individual stimulations were applied in a pseudo-random order, at an interval of 3000 ms, for a total of 1160 repetitions, and a total of less than 1 hour of training.

Initial Synaptic Weights and Initial Connectivity%

All the initial synaptic connections ("*initial weights*") in the network were given a weight between 0.001 and 1 (*initial weights*). No weight could ever exceed 1. As all our networks were fully connected no synapse had 0 weight. The initial weights of the whole population of synapses in the network were generated as log-normal distributions with different mean weights (μ) (values between 0.05 to 0.5) and coefficient of variation (σ_{cv}) (values between 10% - 50%). The variance of the distribution was quantified as (σ) = $(\sigma_{cv}/100) * \mu$ (Fig. S8). 'Initial connectivity%' indicated the mean weight in the network but was also a label we used to indicate the different initial weight distribution parameters (μ and σ_{cv}) (Fig. S9). Within each given parameter combination (initial connectivity%) weights were also randomized to obtain five different versions of each initial connectivity% network.

Synaptic Learning

We used the same Hebbian-inspired '*activity dependent synaptic plasticity rule*' (6) for learning synaptic weights in both excitatory and inhibitory synapses and neurons. The learning rule was formulated to reward the correlation between the individual synaptic activity (a_i) and the neuron activity (A). A positive correlation between the neuron & the synaptic activity leads to potentiation (increase) in synaptic weight and decorrelation between these activities leads to depression (decrease) in synaptic weight. For each stimulus presentation ($t_0 - t_n$), the weight change (Δw) of a synapse (i) was given by equation 7.

$$\Delta w_i = \int_{t_0}^{t_n} \{(A(t) - Th) * a_i(t)\} \ . \eta \ . \xi \tag{7}$$

The value of the integral ($t_n = 1000ms$) determined the magnitude of the individual synaptic weight changes.

To obtain long-term network stability, we also implemented a regulation of the synaptic plasticity that is related to the BCM rule, using a *learning polarity threshold (Th)*. The learning polarity threshold implements an effect

that is related to the BCM rule and defines above what activity level the neuron becomes more likely to depress its afferent synapses, and vice versa (64, 6, 65). The Th was given by equation 8. In this case, we did implement a minor difference between the excitatory and the inhibitory synapses, which led to that the learning polarity threshold was lower for the inhibitory synapses at each given activity level of the postsynaptic neurons (Fig. S14C). This means that the probability of potentiation in the inhibitory synapses was higher for each given neuron activity level, although to a decreasing degree as the neuron activity increased. In particular at low-levels of neuron activity, such as in early stages of learning, this non-linearity enhanced the propagation of excitatory activity through the network.

$$Th = -logn(\mu, \sigma) + A(t) + A_o \tag{8}$$

The strength of potentiation/depression of an individual synaptic weight was also regulated by a learning rate (η) and a compensation factor (ξ). The learning rate was defined as an exponential decay function ($e^{-3.5}$) of the current neuron activity, limiting the rate at which synaptic weight changes occurred (Fig. S14A). The compensation factor constant is given by a sigmoid function (midpoint of 0.5 and steepness of 0.05, Fig. S14B) of current synaptic weight w_i. The compensation factor allowed the weight change of a given synapses to become higher if its current weight was low and vice versa. This factor is motivated by that the insertion of a synaptic receptor in the synaptic membrane can be regarded as a chemical reaction (the insertion and removal of synaptic receptors is handled by partly separate chemical reactions (66)), where the addition of a new channel will become less likely the higher the number of ion channels already inserted and vice versa (8). The compensation factor function was flipped for depression and potentiation of a synapse (Fig. S14B). The weight change (Δw_i) and learning polarity threshold (*Th*) were computed as moving averages across 100 stimulus presentations in order to dampen their rates of adaptation.

Excitatory Synapse Learning Signal Filter

In general, the excitatory and inhibitory synapses learned using the same Hebbian-like learning rule, based on their activity correlation with the postsynaptic neuron. But for the densest network, this proved to not work as well as for the less densely connected networks, and we therefore implemented a tweak where the excitatory synapse learning was instead based on correlation with a high-pass filtered version of the postsynaptic neuron activity. The purpose was to make the excitatory synapse learning more selective, i.e. it would only correlate with positive changes in the postsynaptic activity. This could for example equal that the the postsynaptic activity in the dendritic spine, or the synaptic subspace underneath the excitatory synapse, would only be exposed to or only react to positive *changes* in the calcium activity of the main compartment of the neuron. Biological studies indicate that the near-synaptic calcium concentration can have different time constants than the calcium concentration in the main compartment of the neuron (67, 68, 69) and specific dynamics in the calcium concentration could impact synaptic plasticity (64). In order to achieve a high-pass filtered version of the postsynaptic activity (A), with which the excitatory synapse activity was correlated to obtain a net weight change, we multiplied that activity with an exponential function (e^x) (Fig. 4C) with different order *x*. This filter was applied only on excitatory synaptic activity (a_i) during the learning phase, in the analysis of Figures 4C,D, S15, S16.

Network Performance (Post-learning)

To evaluate the learning performance of the networks studied, we compared the generalization and the robustness capabilities of the skin networks and the Gaussian networks (Fig. 2). In order to test the generalization, we quantified the classification accuracy across five naive skin stimuli (Fig. S1F - J) and 11 force impulse skin stimuli (Fig. S3), neither of which were used during the learning process (Fig. 2D, F). In order to test the robustness capabilities we quantified the classification accuracy across the naive and force impulse input, by randomly removing two sensor input synapses, corresponding to 20% of the total sensor input to the network. The classification performance was quantified for four noise levels, where a random noise of a given signal-to-noise ratio (snr) was added to the activities of each neuron. We reported the average classification performance for 10 different repetitions of each noise level. The classification accuracy for each noise level was further reported for five different skin & Gaussian networks, *i.e.* networks that had five different random initial weights (within the constraints indicated by the initial connectivity% label), and the distribution of the classification performance across these random initial weights was reported.

Statistical Analysis

Total Weight change

Total weight change (ΔW) within a neuron is defined as the summed difference between all the initial weights (W_i^I, pre-learning) and their respective end-weights (W_i^E, post-learning) as given by equation 9. Where, m is total number of neurons (j) and n is total number of synaptic weights (i) for a given neuron. The average synaptic weight changes across all the neurons was reported in Fig. 3F-I, S12, S13, S16.

$$\Delta W = \frac{1}{m}\sum_{j=1}^{m}\left(\sum_{i=1}^{n}\left(\mathrm{W}_i^E - \mathrm{W}_i^I\right)\right) \tag{9}$$

Cross-correlation

The correlation index measure was used to compute the similarity in the neuronal activities during test inputs. The correlation between two neurons was computed with an inbuilt MATLAB function "*xcorr*" (with zero lag), which produces values from 0 (uncorrelated) to 1 (identical). This pairwise cross correlation was calculated across all neuron pairs and the average value was reported (Fig. 4A-B, S17, S15).

Frequency analysis

A continuous wavelet transform (using an inbuilt MATLAB function "*cwt*") was performed in order to define the frequency composition of the input sensory responses over time. The wavelet transform was used to extract the power of each frequency band as a function of time for the time-continuous responses of the sensors. Here, we reported (Fig. S2), for each frequency band, the maximum power of each sensor across ≈ 1160 stimulus presentations.

Principal component analysis (PCA)

Principal component analysis was performed on the actvitiy of the excitatory neurons using an inbuilt MATLAB function *pca*. The pca function projects the neuron activity onto principal component space (new set of variables, Principal Components (PCs)) that explain the high dimensional input data on fewer output dimensions while encompassing the maximum preservation of information in the input data. The product between the neuron activity and PC coefficients results in "*PC scores*" that represent the sensory signals in PC space (Fig. 2C, E).

Classification

To quantify the classification accuracy across different skin inputs (Fig. 2D, F) we used a linear tree classifier. The excitatory neuron population activity for each given skin input at each defined level of network noise was projected onto the first PC and the PC scores (see section above) were used as input observations to the classifier. Each skin input was repeated for 50 times, where the neuronal noise resulted in different responses for each repetition. The data to the classifier was binned into 5 classes while testing the 5 naive skin inputs (50 repetitions x 5 classes = 250 observations), and 11 classes while testing the 11 force impulse inputs (50 repetitions x 11 classes = 550 observations). As each response consisted of 3000 time steps, the classifier had 3000 predictors for each observation. The classifier was trained and tested using a 5-fold cross-validation, which was repeated for 100 iterations to ensure robustness. This analysis was performed using a Matlab toolbox "*Classification Learner*".

Data Availability

The full set of simulation data used to produce all of the results in this paper is available from the authors upon reviewers request and at publication.

References

[1] Zador, A. et al. Catalyzing next-generation artificial intelligence through neuroai. Nature communications **14**, 1597 (2023).

[2] Rongala, U. B., Seyfarth, A., Hayward, V. & Jörntell, H. The import of skin tissue dynamics in tactile sensing. Cell Reports Physical Science (2024).

[3] Seyfarth, A., Zhao, G. & Jörntell, H. Whole body coordination for self-assistance in locomotion. Frontiers in Neurorobotics **16**, 883641 (2022).

[4] Hayward, V. Is there a 'plenhaptic'function? Philosophical Transactions of the Royal Society B: Biological Sciences **366**, 3115–3122 (2011).

[5] Jörntell, H. et al. Segregation of tactile input features in neurons of the cuneate nucleus. Neuron **83**, 1444–1452 (2014).

[6] Rongala, U. B. et al. Intracellular dynamics in cuneate nucleus neurons support self-stabilizing learning of generalizable tactile representations. Frontiers in cellular neuroscience **12**, 210 (2018).

[7] Suryanarayana, S. M., Robertson, B., Wallén, P. & Grillner, S. The lamprey pallium provides a blueprint of the mammalian layered cortex. Current Biology **27**, 3264–3277 (2017).

[8] Rongala, U. B., Enander, J. M., Kohler, M., Loeb, G. E. & Jörntell, H. A non-spiking neuron model with dynamic leak to avoid instability in recurrent networks. Frontiers in computational neuroscience **15** (2021).

[9] Binzegger, T., Douglas, R. J. & Martin, K. A. A quantitative map of the circuit of cat primary visual cortex. Journal of Neuroscience **24**, 8441–8453 (2004).

[10] Song, S., Sjöström, P. J., Reigl, M., Nelson, S. & Chklovskii, D. B. Highly nonrandom features of synaptic connectivity in local cortical circuits. PLoS biology **3**, e68 (2005).

[11] Koestinger, G., Martin, K. A. & Rusch, E. S. Translaminar circuits formed by the pyramidal cells in the superficial layers of cat visual cortex. Brain Structure and Function **223**, 1811–1828 (2018).

[12] Kar, K. & DiCarlo, J. J. Fast recurrent processing via ventrolateral prefrontal cortex is needed by the primate ventral stream for robust core visual object recognition. Neuron **109**, 164–176 (2021).

[13] Douglas, R., Koch, C., Mahowald, M. & Martin, K. The role of recurrent excitation in neocortical circuits. In Models of cortical circuits, 251–282 (Springer, 1999).

[14] Kalisman, N., Silberberg, G. & Markram, H. The neocortical microcircuit as a tabula rasa. Proceedings of the National Academy of Sciences **102**, 880–885 (2005).

[15] Binzegger, T., Douglas, R. J. & Martin, K. A. Topology and dynamics of the canonical circuit of cat v1. Neural Networks **22**, 1071–1078 (2009).

[16] Zhu, J. J. & Lo, F.-S. Recurrent inhibitory circuitry in the deep layers of the rabbit superior colliculus. The Journal of Physiology **523**, 731–740 (2000).

[17] Douglas, R. J. & Martin, K. A. Inhibition in cortical circuits. Current biology **19**, R398–R402 (2009).

[18] Obermayer, J. et al. Lateral inhibition by martinotti interneurons is facilitated by cholinergic inputs in human and mouse neocortex. Nature communications **9**, 1–14 (2018).

[19] Swadlow, H. A. Fast-spike interneurons and feedforward inhibition in awake sensory neocortex. Cerebral Cortex **13**, 25–32 (2003).

[20] Isaacson, J. S. & Scanziani, M. How inhibition shapes cortical activity. Neuron **72**, 231–243 (2011).

[21] Jörntell, H. & Ekerot, C.-F. Receptive field plasticity profoundly alters the cutaneous parallel fiber synaptic input to cerebellar interneurons in vivo. Journal of Neuroscience **23**, 9620–9631 (2003).

[22] Pi, H.-J. et al. Cortical interneurons that specialize in disinhibitory control. Nature **503**, 521–524 (2013).

[23] Sultan, K. T. & Shi, S.-H. Generation of diverse cortical inhibitory interneurons. Wiley Interdisciplinary Reviews: Developmental Biology **7**, e306 (2018).

[24] Cardin, J. A. Inhibitory interneurons regulate temporal precision and correlations in cortical circuits. Trends in neurosciences **41**, 689–700 (2018).

[25] Hafner, G. et al. Mapping brain-wide afferent inputs of parvalbumin-expressing gabaergic neurons in barrel cortex reveals local and long-range circuit motifs. Cell reports **28**, 3450–3461 (2019).

[26] Luo, P. et al. Whole brain mapping of long-range direct input to glutamatergic and gabaergic neurons in motor cortex. Frontiers in neuroanatomy **13**, 44 (2019).

[27] Ährlund-Richter, S. et al. A whole-brain atlas of monosynaptic input targeting four different cell types in the medial prefrontal cortex of the mouse. Nature neuroscience **22**, 657–668 (2019).

[28] Wall, N. R. et al. Brain-wide maps of synaptic input to cortical interneurons. Journal of Neuroscience **36**, 4000–4009 (2016).

[29] Robinson, S. R., Blumberg, M. S., Lane, M. S. & Kreber, L. S. Spontaneous motor activity in fetal and infant rats is organized into discrete multilimb bouts. Behavioral neuroscience **114**, 328 (2000).

[30] Blumberg, M. S., Marques, H. G. & Iida, F. Twitching in sensorimotor development from sleeping rats to robots. Current Biology **23**, R532–R537 (2013).

[31] Gauthier, D. J., Bollt, E., Griffith, A. & Barbosa, W. A. Next generation reservoir computing. Nature communications **12**, 1–8 (2021).

[32] Faisal, A. A., Selen, L. P. & Wolpert, D. M. Noise in the nervous system. Nature reviews neuroscience **9**, 292–303 (2008).

[33] Nilsson, M. N. & Jörntell, H. Channel current fluctuations conclusively explain neuronal encoding of internal potential into spike trains. Physical Review E **103**, 022407 (2021).

[34] Oddo, C. M. et al. Artificial spatiotemporal touch inputs reveal complementary decoding in neocortical neurons. Scientific reports **7**, 1–17 (2017).

[35] Kristensen, S. S., Kesgin, K. & Jörntell, H. High-dimensional cortical signals reveal rich bimodal and working memory-like representations among s1 neuron populations. Communications Biology **7**, 1043 (2024).

[36] Kristensen, S. S. & Jörntell, H. Differential encoding of temporally evolving color patterns across nearby v1 neurons. Frontiers in Cellular Neuroscience **17** (2023).

[37] Mogensen, H., Norrlid, J., Enander, J. M., Wahlbom, A. & Jörntell, H. Absence of repetitive correlation patterns between pairs of adjacent neocortical neurons in vivo. Frontiers in neural circuits **13**, 48 (2019).

[38] Stringer, C. et al. Spontaneous behaviors drive multidimensional, brainwide activity. Science **364**, eaav7893 (2019).

[39] Stringer, C., Michaelos, M., Tsyboulski, D., Lindo, S. E. & Pachitariu, M. High-precision coding in visual cortex. Cell **184**, 2767–2778 (2021).

[40] Klushyn, A., Kurle, R., Soelch, M., Cseke, B. & van der Smagt, P. Latent matters: Learning deep state-space models. Advances in Neural Information Processing Systems **34**, 10234–10245 (2021).

[41] McKinney, R. A. Excitatory amino acid involvement in dendritic spine formation, maintenance and remodelling. The Journal of physiology **588**, 107–116 (2010).

[42] Gibson, E. J. Exploratory behavior in the development of perceiving, acting, and the acquiring of knowledge. Annual review of psychology **39**, 1–42 (1988).

[43] Enander, J. M. et al. A model for self-organization of sensorimotor function: the spinal monosynaptic loop. Journal of Neurophysiology **127**, 1460–1477 (2022).

[44] Enander, J. M., Loeb, G. E. & Jörntell, H. A model for self-organization of sensorimotor function: spinal interneuronal integration. Journal of Neurophysiology **127**, 1478–1495 (2022).

[45] Friston, K. The free-energy principle: a rough guide to the brain? Trends in cognitive sciences **13**, 293–301 (2009).

[46] Clark, A. Whatever next? predictive brains, situated agents, and the future of cognitive science. Behavioral and brain sciences **36**, 181–204 (2013).

[47] Rao, R. P. A sensory–motor theory of the neocortex. Nature Neuroscience 1–15 (2024).

[48] Hennequin, G., Agnes, E. J. & Vogels, T. P. Inhibitory plasticity: balance, control, and codependence. Annual review of neuroscience **40**, 557–579 (2017).

[49] Mackwood, O., Naumann, L. B. & Sprekeler, H. Learning excitatory-inhibitory neuronal assemblies in recurrent networks. Elife **10**, e59715 (2021).

[50] Vogels, T. P., Sprekeler, H., Zenke, F., Clopath, C. & Gerstner, W. Inhibitory plasticity balances excitation and inhibition in sensory pathways and memory networks. Science **334**, 1569–1573 (2011).

[51] Clopath, C., Vogels, T. P., Froemke, R. C. & Sprekeler, H. Receptive field formation by interacting excitatory and inhibitory synaptic plasticity. BioRxiv **xxx**, 066589 (2016).

[52] Rubin, R., Abbott, L. & Sompolinsky, H. Balanced excitation and inhibition are required for high-capacity, noise-robust neuronal selectivity. Proceedings of the National Academy of Sciences **114**, E9366–E9375 (2017).

[53] Weber, S. N. & Sprekeler, H. Learning place cells, grid cells and invariances with excitatory and inhibitory plasticity. Elife **7**, e34560 (2018).

[54] Rupprecht, P. & Friedrich, R. W. Precise synaptic balance in the zebrafish homolog of olfactory cortex. Neuron **100**, 669–683 (2018).

[55] Vogels, T. P. & Abbott, L. Gating multiple signals through detailed balance of excitation and inhibition in spiking networks. Nature neuroscience **12**, 483–491 (2009).

[56] Hennequin, G., Vogels, T. P. & Gerstner, W. Optimal control of transient dynamics in balanced networks supports generation of complex movements. Neuron **82**, 1394–1406 (2014).

[57] Denève, S. & Machens, C. K. Efficient codes and balanced networks. Nature neuroscience **19**, 375–382 (2016).

[58] Najafi, M., McMenamin, B. W., Simon, J. Z. & Pessoa, L. Overlapping communities reveal rich structure in large-scale brain networks during rest and task conditions. Neuroimage **135**, 92–106 (2016).

[59] Wiertlewski, M. & Hayward, V. Mechanical behavior of the fingertip in the range of frequencies and displacements relevant to touch. Journal of biomechanics **45**, 1869–1874 (2012).

[60] Shao, Y., Hayward, V. & Visell, Y. Spatial patterns of cutaneous vibration during whole-hand haptic interactions. Proceedings of the National Academy of Sciences **113**, 4188–4193 (2016).

[61] Shao, Y., Hayward, V. & Visell, Y. Compression of dynamic tactile information in the human hand. Science Advances **6**, eaaz1158 (2020).

[62] Hayward, V. et al. Spatio-temporal skin strain distributions evoke low variability spike responses in cuneate neurons. Journal of The Royal Society Interface **11**, 20131015 (2014).

[63] Inman, D. J. Vibration with control (John Wiley & Sons, 2017).

[64] Graupner, M. & Brunel, N. Calcium-based plasticity model explains sensitivity of synaptic changes to spike pattern, rate, and dendritic location. Proceedings of the National Academy of Sciences **109**, 3991–3996 (2012).

[65] Rongala, U. B., Mazzoni, A., Spanne, A., Jörntell, H. & Oddo, C. M. Cuneate spiking neural network learning to classify naturalistic texture stimuli under varying sensing conditions. Neural Networks **123**, 273–287 (2020).

[66] Jörntell, H. & Hansel, C. Synaptic memories upside down: bidirectional plasticity at cerebellar parallel fiber-purkinje cell synapses. Neuron **52**, 227–238 (2006).

[67] Wang, S. S.-H., Denk, W. & Häusser, M. Coincidence detection in single dendritic spines mediated by calcium release. Nature neuroscience **3**, 1266–1273 (2000).

[68] Isope, P. & Murphy, T. H. Low threshold calcium currents in rat cerebellar purkinje cell dendritic spines are mediated by t-type calcium channels. The Journal of physiology **562**, 257–269 (2005).

[69] Tigaret, C. M., Olivo, V., Sadowski, J. H., Ashby, M. C. & Mellor, J. R. Coordinated activation of distinct ca2+ sources and metabotropic glutamate receptors encodes hebbian synaptic plasticity. Nature communications **7**, 1–14 (2016).

[70] Yin, P., Esser, E. & Xin, J. Ratio and difference of l_1 and l_2 norms and sparse representation with coherent dictionaries. Communications in Information and Systems **14**, 87–109 (2014).

Acknowledgements

This work was supported by the EU Grant FET 829186 ph-coding (Predictive Haptic COding Devices In Next Generation interfaces), the Swedish Research Council (Project Grant No. K2014-63X-14780-12-3).)

Author Information

Contributions

U.B.R. and H.J., designed and performed the research.

Competing Interests

The authors declare that they have no competing interests.

Correspondence

Correspondence and requests for materials should be addressed to
Udaya B Rongala (email: udaya_bhaskar.rongala@med.lu.se) and Henrik Jörntell (email: henrik.jorntell@med.lu.se)

Supplementary Material

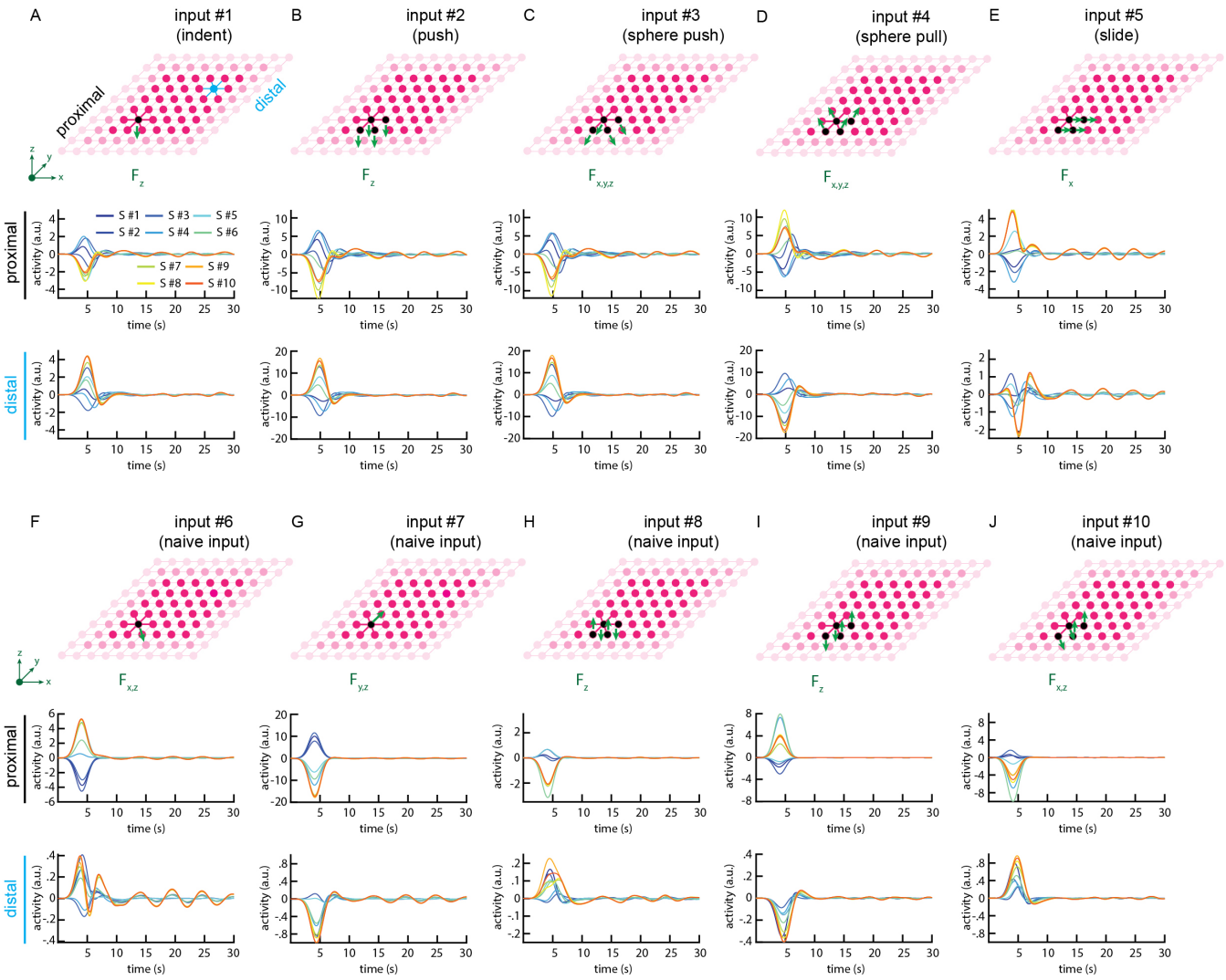

Supplementary Figure 1: Skin sensor responses (spring forces) from the 10 springs attached to the proximal (node colored in black) (used as S#1 - S#10 for the network training) as well as 10 springs attached to a distal node (node colored in blue). The responses of the two population of sensors were shown separately for each input. Note that each input had the same duration but differed with respect to the spatial force distribution along the x-/y-/z-axes ($[f_x f_y f_z]$, as indicated by the green arrows). (**A-E**) The five stimuli used for network learning. (**F-J**) The naive stimuli used for testing generalization capabilities in Fig. 2. Note that the actual skin model was composed of more nodes than illustrated in the display.

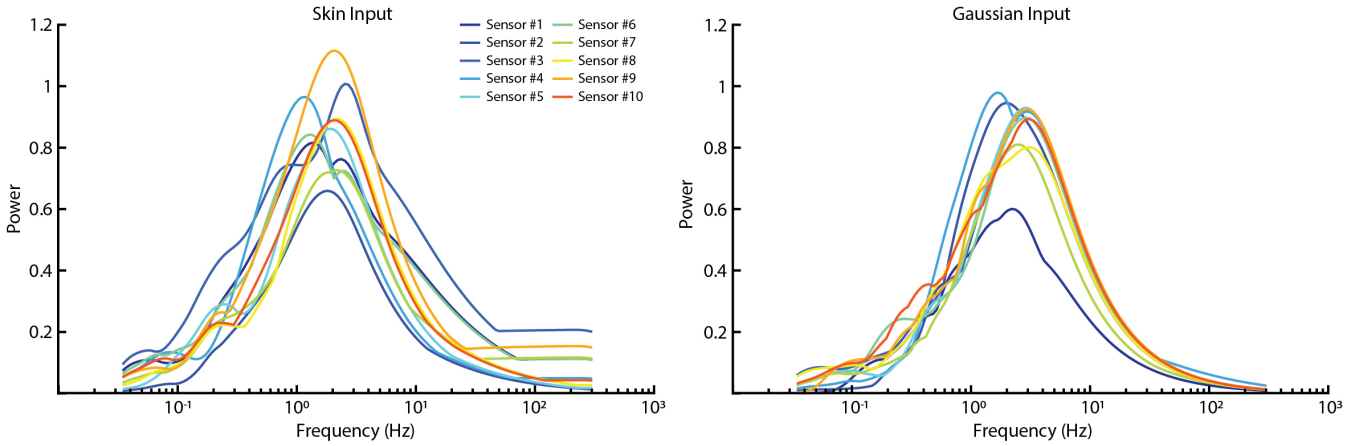

Supplementary Figure 2: Frequency power distribution of all ten skin and Gaussian sensory inputs, averaged across 3500 stimulus presentations.

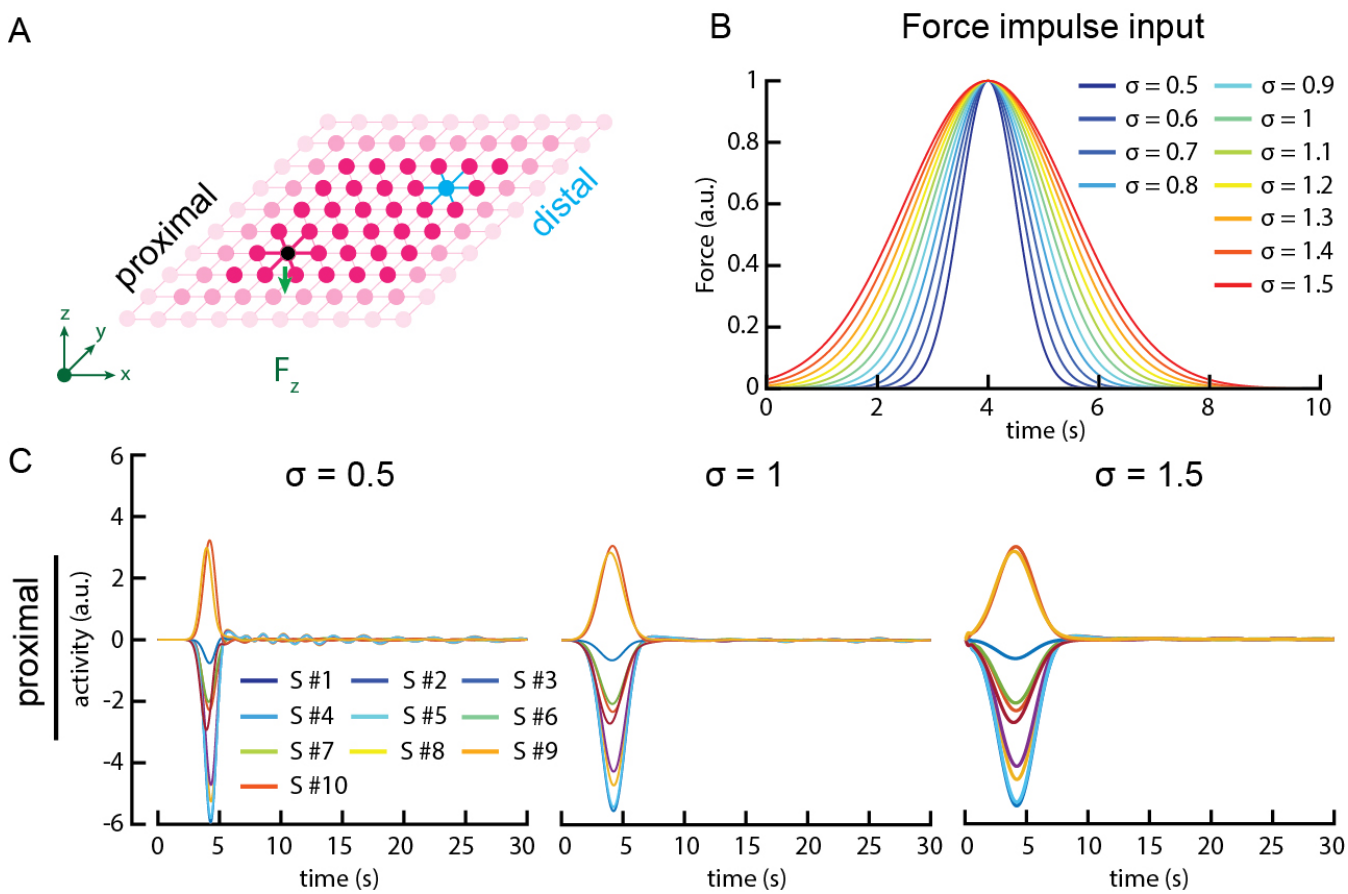

Supplementary Figure 3: The force impulse input consisted of applying a time-evolving force to one mass only. The mass in black was impacted by a force in the z direction (A). (B) The force was applied with a Gaussian function, and force impulses differed solely by the sigma of their temporal Gaussian function. This contrasted with the skin inputs for which the temporal Gaussian function was always the same (σ=1). (C) Example responses of the proximal sensors, i.e. the 10 sensors connected to the proximal mass.

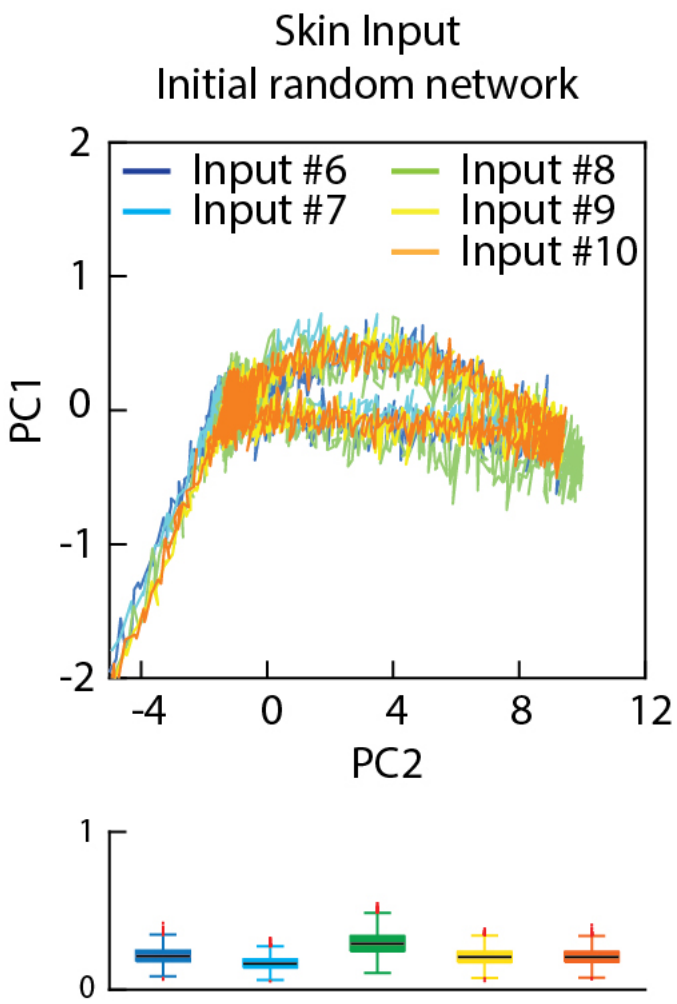

Supplementary Figure 4: **Projection of the neuron population activity from the pre-learning random network onto principal component space.** The output of the neuron population for five different naive skin inputs (Fig. 1F-J) projected on the first two principal components (PCs) (at a neuronal noise level of 0.1, same as in Fig. 2C,E). Inset: the variance of the PCs across the 50 different initial noise randomizations.

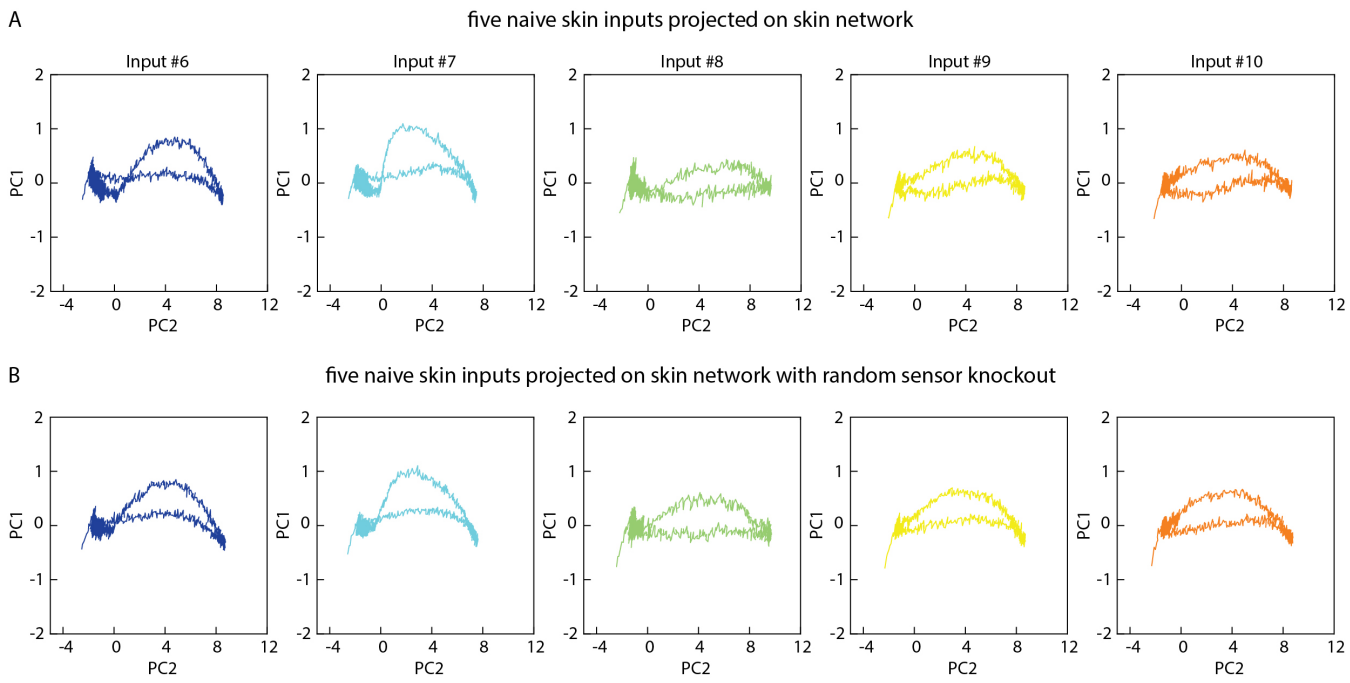

Supplementary Figure 5: **Effect of sensory knockout on the neuron population activity in the skin network.** (**A**) The output of the neuron population for five different naive skin inputs (Fig. 1F-J) projected on the first two principal components (PCs). The plots illustrate outputs for the skin networks (same plots as in Fig. 2C, but here shown separately for each input rather than superimposed). (**B**) Similar display as in **A**, but with 'knock-out' of two random skin sensors post-learning.

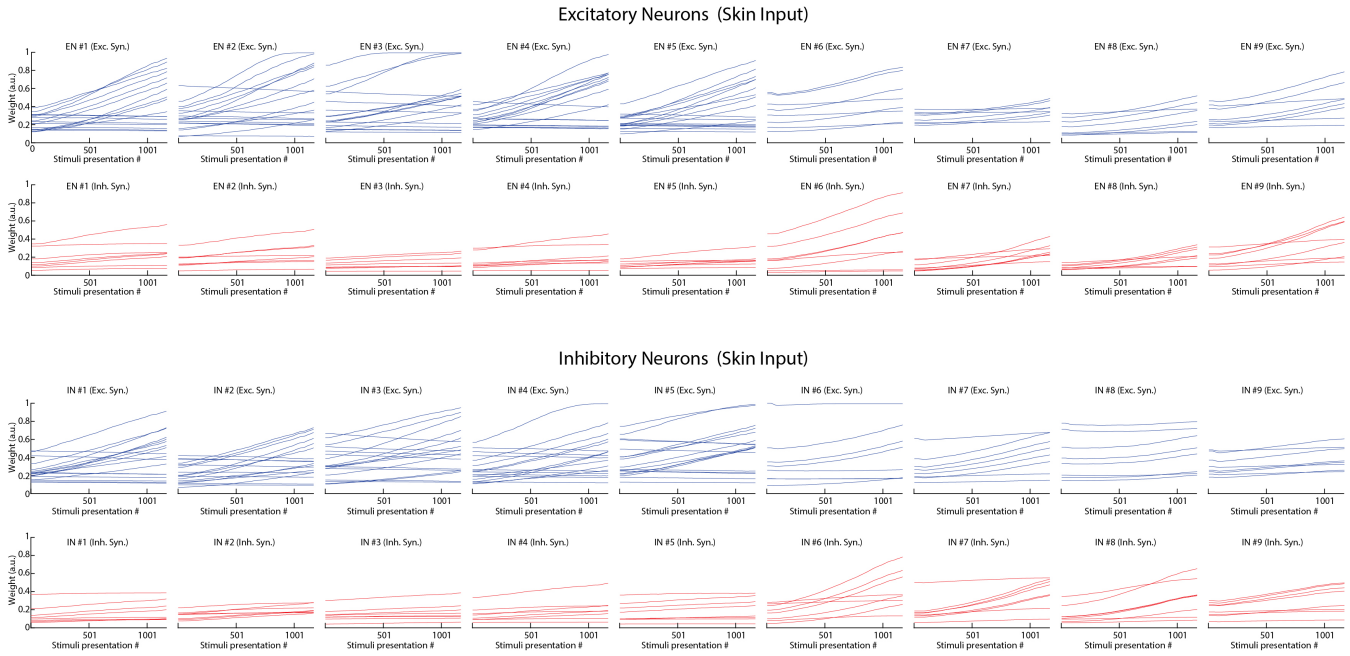

Supplementary Figure 6: Excitatory and inhibitory synaptic weight evolution across all 18 neurons (9 EN & 9 IN) in the network, for learning based on skin inputs. The initial weights (weight distribution at stimulus presentation #1) correspond to the weights matrix in Fig. 3A. The end weights correspond to the weight matrix in Fig. 3B

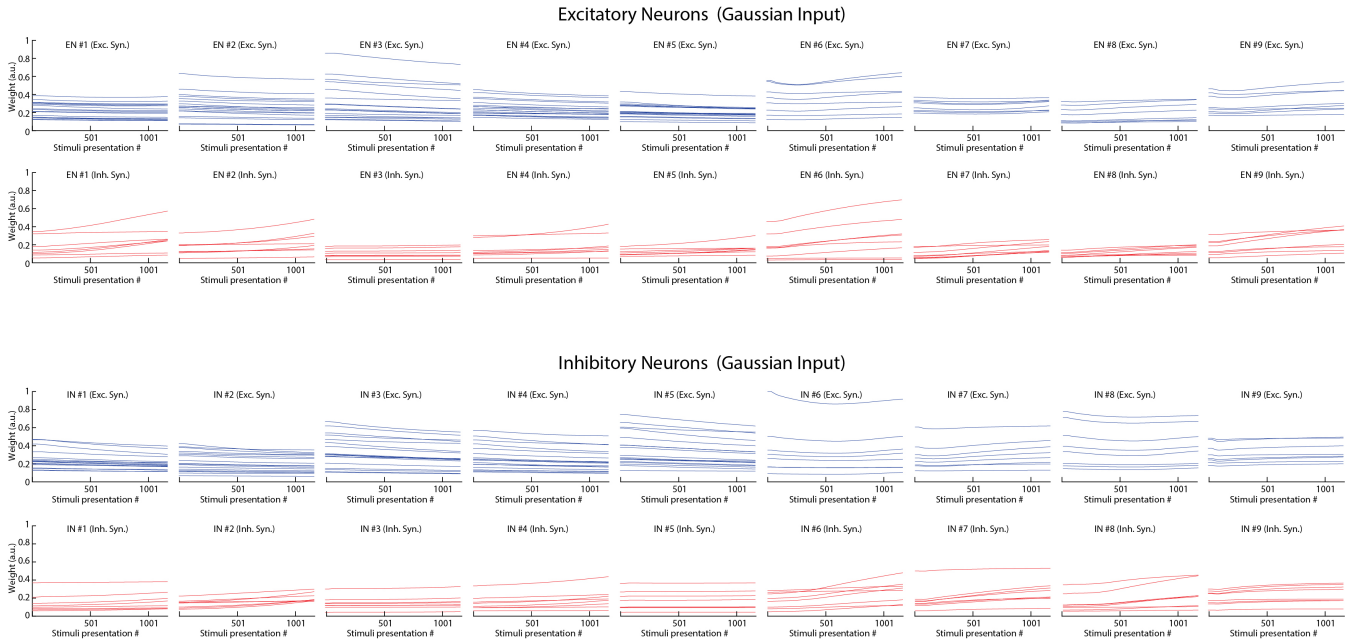

Supplementary Figure 7: Excitatory and inhibitory synaptic weight evolution across all 18 neurons (9 ENs & 9 INs) in the network, for learning based on Gaussian inputs. The initial weights (weight distribution at stimulus presentation #1) correspond to the weights matrix in Fig. 3A. The end weights correspond to the weight matrix in Fig. 3C.

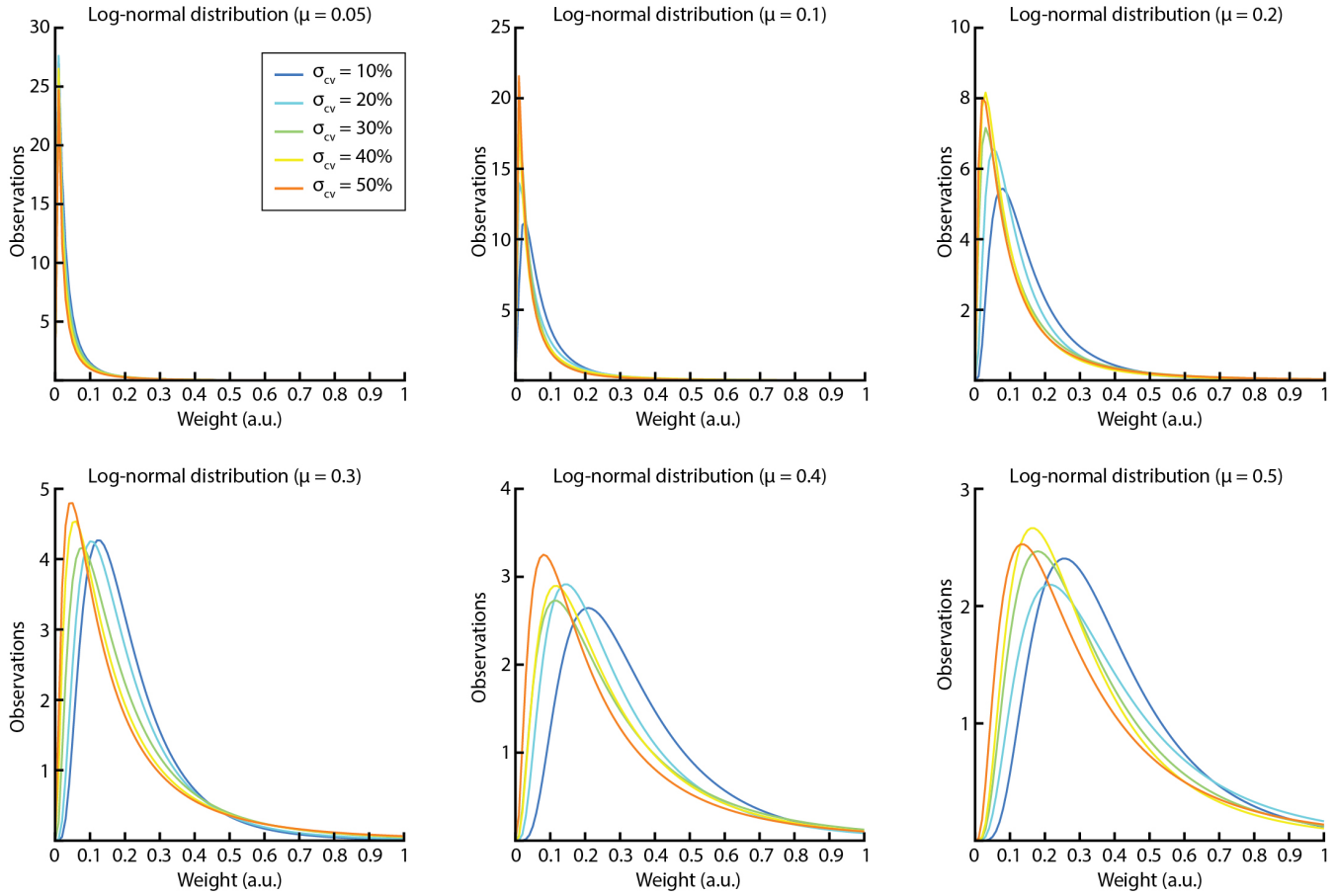

Supplementary Figure 8: The 30 different initial weight settings tested. We used six different mean weights (μ; ranging between 0.05 & 0.5). For each mean weight, we used five different levels of synaptic weight spread, expressed as a the coefficient of variation (σ_{cv}, ranging between 10% & 50%). The variance of the distribution of the initial weights was instead (σ) = $(\sigma_{cv}/100) * \mu$. Each of the 30 different initial weight settings had its own randomization across the synapses, the numbers presented here only illustrates the data at the synaptic population level.

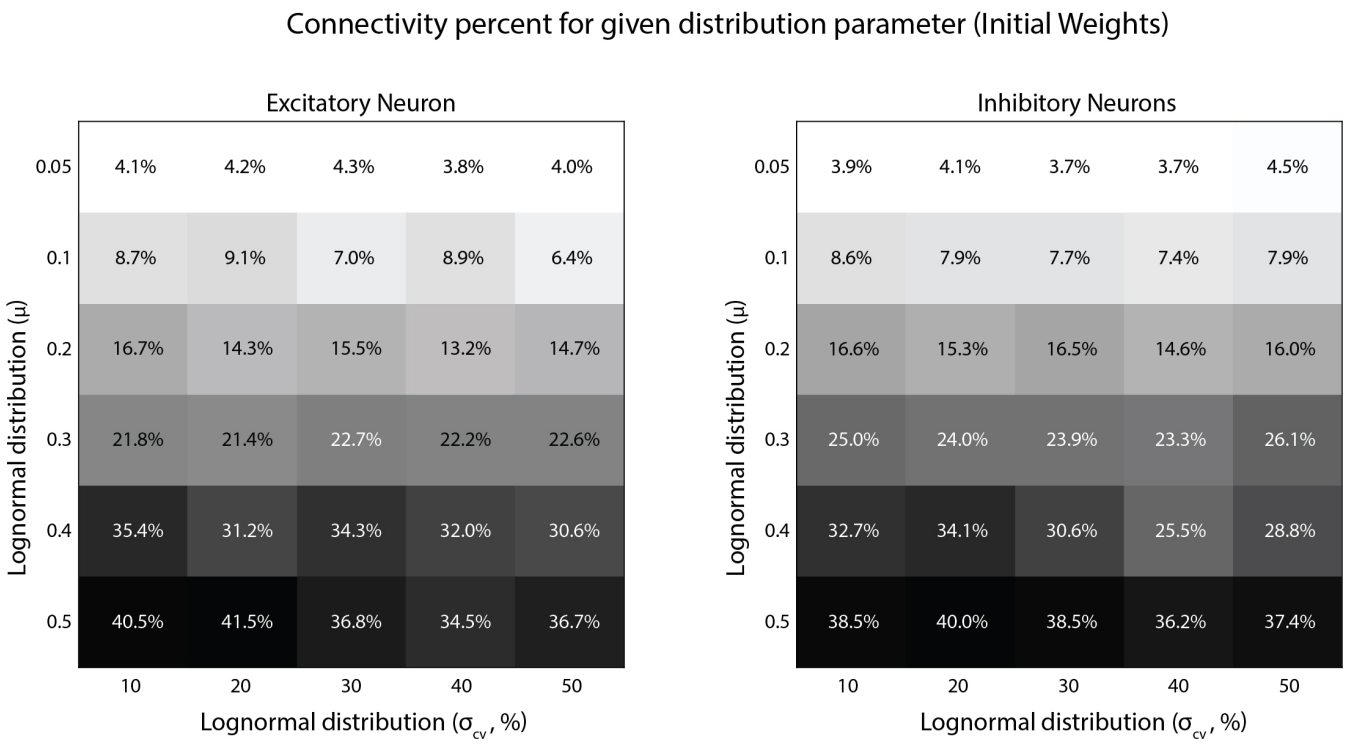

Supplementary Figure 9: Network parameter settings for each specific Initial Connectivity% label. μ and σ_{cv} refers to the distributions in Fig. S8. $Connectivity\% = \sum\ initial\ weights\ /\ number\ of\ synapses.$

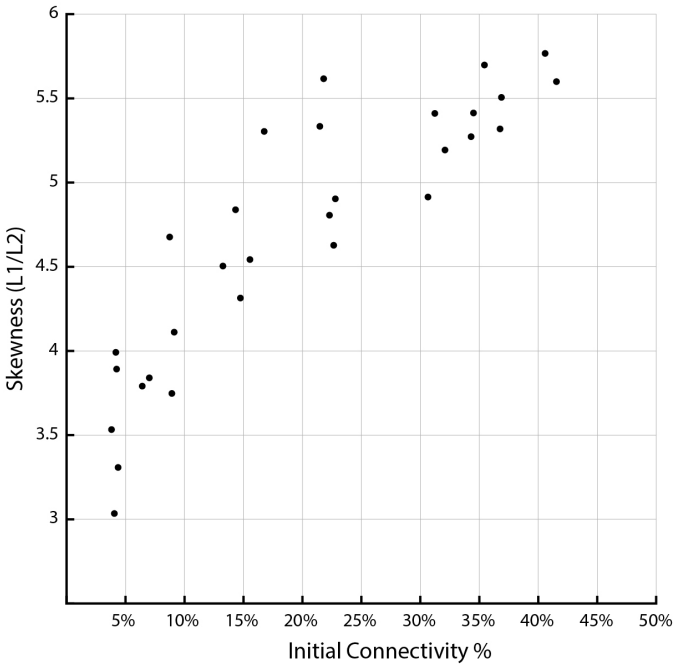

Supplementary Figure 10: The skewness of initial synaptic weight distribution for a given connectivity %. The synaptic weight skewness was calculated as the ratio between the *l1* and *l2* norm of the weight vector (70). This measure will report its minimal value when all synapses have the same weight and a maximum value when one synapse has maximum weight and all other synapses have zero weight.

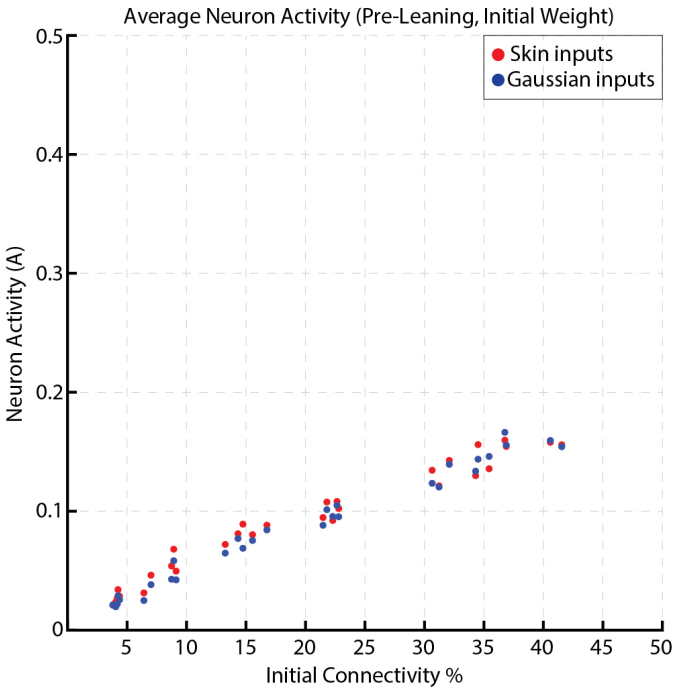

Supplementary Figure 11: The average activity across all the neurons in the network for a given initial weight connectivity % and multiple sensory inputs (skin input & Gaussian input)

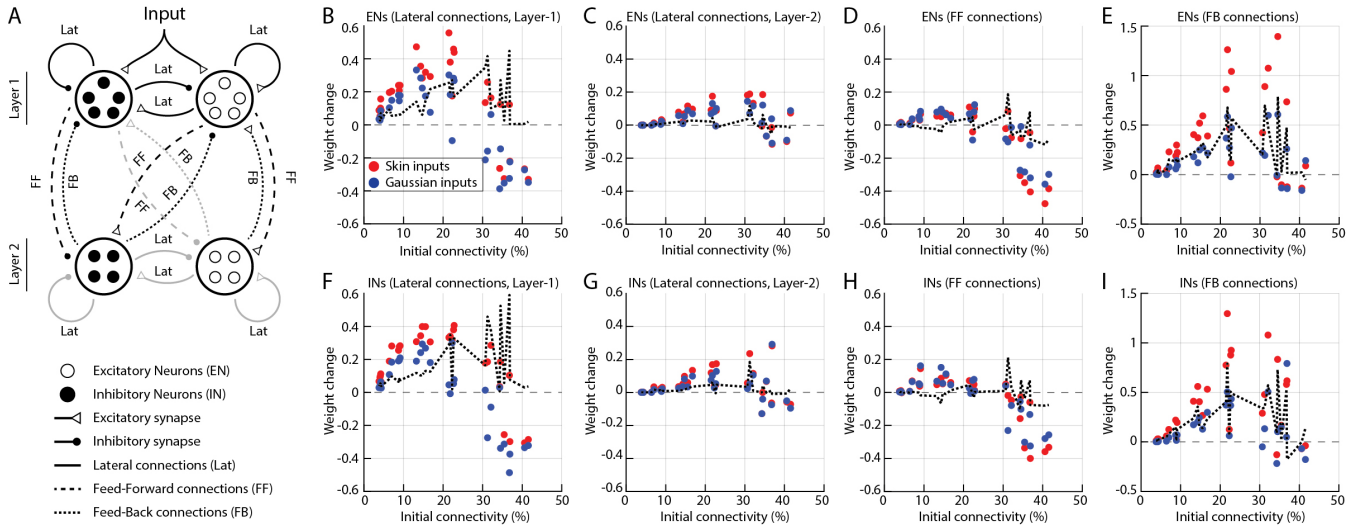

Supplementary Figure 12: **Synaptic weight changes resulting from learning for specific subtypes of synaptic connections.** Same display conventions as in Fig. 3. (**A**) Schematic of the fully connected network structure studied; with specific labels for each type of connection. "*Lat*": Lateral connections within a layer, "*FF*": feed-forward connections from neurons in layer 1 to neurons in layer 2, "*FB*": feed-back connections from neurons in layer 2 to neurons in layer 1. (**B**) Weight changes across all the excitatory and inhibitory lateral synaptic connections on excitatory neurons (*EN*) in layer 1. (**C**) Weight changes across all the lateral synapses on excitatory neurons in layer 2. (**D**) Weight changes across all the feed-forward synapses on excitatory neurons in layer 2. (**E**) Weight changes across all the feedback synapses on excitatory neurons in layer 1. (**F-I**) Weight change analysis similar to that in **B-E**, but instead for synaptic connections made on inhibitory neurons (*IN*). Overall, as in Fig. 3 the weights of all types of synaptic connections tended to increase, up to a certain level of mean initial connectivity (30%), above which the weights instead was decreased by the training. Across all conditions, except for the FF connections the weights increased more with the Skin input than with the Gaussian input (black dashed lines indicates the net difference between the two input conditions).

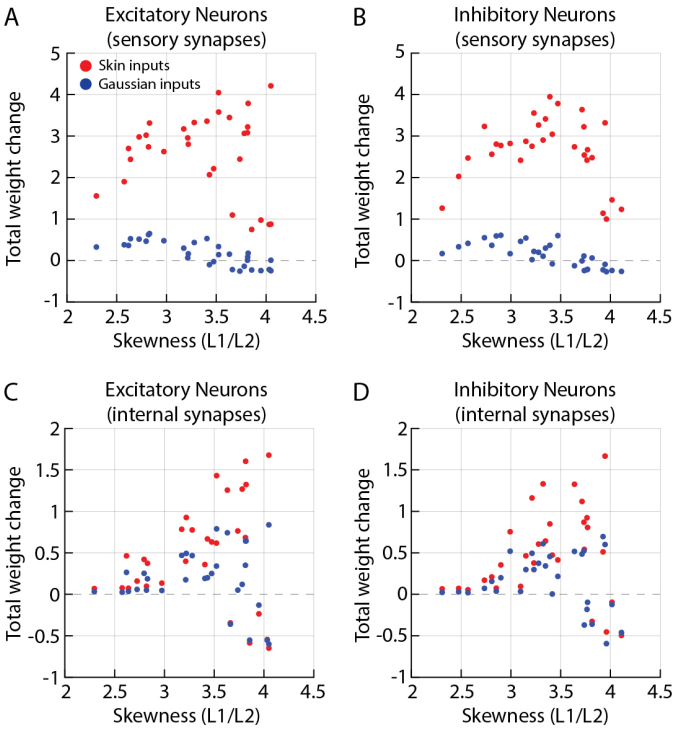

Supplementary Figure 13: **Effects of learning on synaptic weights.** (**A**-**D**) The panels display average weight changes between pre-/post-learning, across all synapses of the indicated category (sensory synapses in **A**, **B** *and* internal synapses in **C**, **D**) for networks with varying skewness of initial synaptic weight distribution (Fig. S10) and sensory input type. Red markers indicate weight change within networks trained on skin inputs and blue markers for corresponding networks trained on Gaussian inputs. (**A**) Weight changes of the sensory synapses on ENs. (**B**) Weight changes of the sensory synapses on INs. (**C**) Weight changes of all excitatory and inhibitory internal synapses on ENs. (**D**) Weight changes of all excitatory and inhibitory internal synapses on INs.

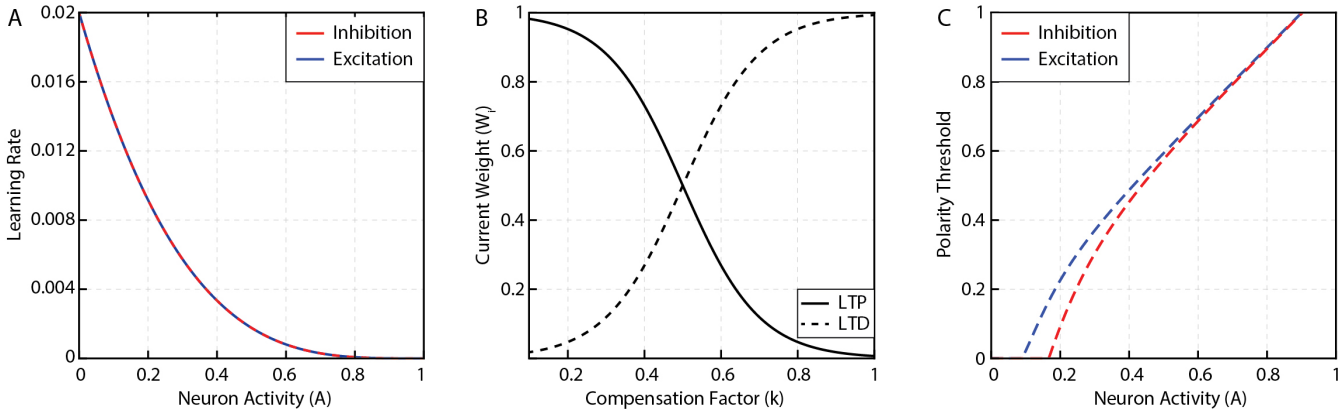

Supplementary Figure 14: Illustration of multiple functions used for synaptic learning process in this study. (**A**) Learning rate as a function of neuron activity (A). (**B**) Compensation factor as function of current synaptic weight (W_i). (**C**) Learning polarity threshold as a function of neuron activity (A).

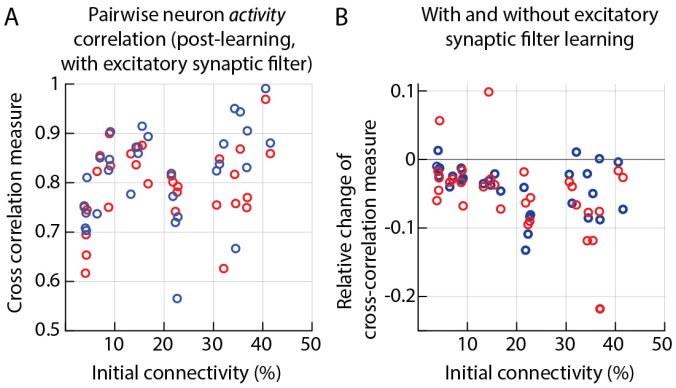

Supplementary Figure 15: **Effect of the excitatory synaptic learning signal filter on the neuronal cross-correlation.**(**A**) Average pairwise cross-correlation measure across all the ENs activity in a network post-learning with excitatory synaptic learning signal filter of $e^{1.4}$ (dotted vertical line in (Fig. 4C)), for networks with different initial connectivity and sensory inputs. (**B**) Net change in the cross-correlation measure of excitatory neuron activity caused by the learning signal filter (difference between (**A**) and Fig. 4B).

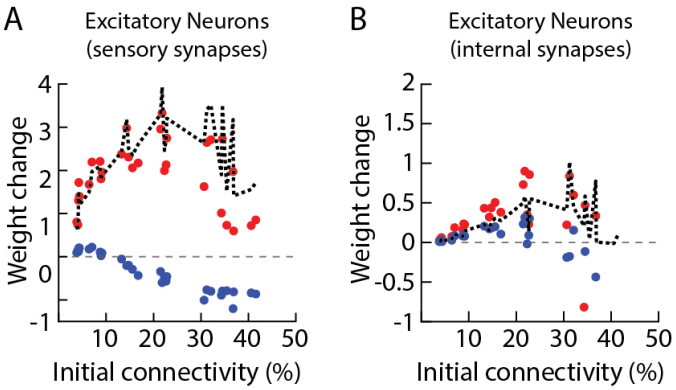

Supplementary Figure 16: **Effect of excitatory synaptic learning signal filter on synaptic weights.** (**A**) Weight change across all the sensory synapses that project as excitatory synaptic connections on excitatory neurons in layer 1 for networks with different initial weight configurations. (**B**) Weight change across all the internal synapses that project as excitatory and inhibitory synaptic connections on all the excitatory neurons within the network. *Note:* **A & B** All networks were trained with the same excitatory synapse learning signal filter of $e^{1.4}$ indicated by the vertical dotted line in Fig. 4B.

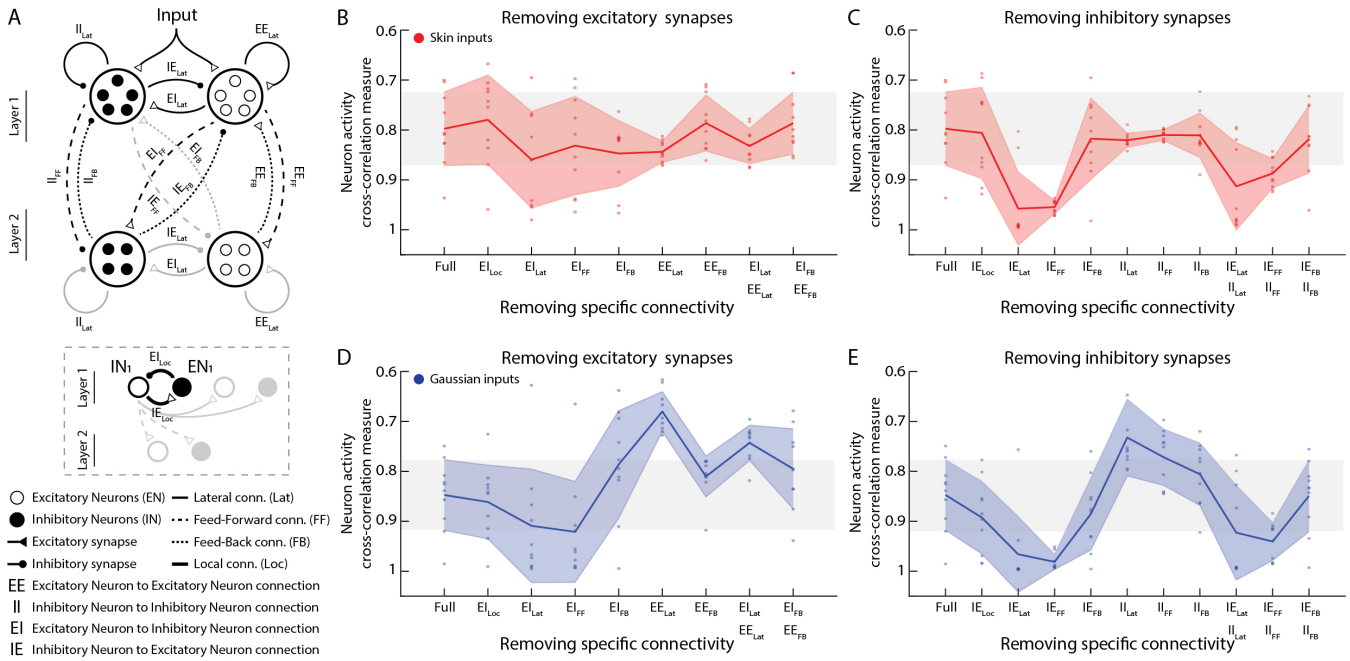

Supplementary Figure 17: **Impact of removing specific synaptic connections on learning quality.** (**A**) Schematic of the fully connected network structure studied; with the insert showing specific labels for the type of individual excitatory and inhibitory synaptic connections between excitatory (ENs) and inhibitory neurons (INs). (**B**) The impact of removing specific types of outgoing excitatory neuron synaptic connections on the learning quality, as indicated by the average pairwise cross correlation measure post-learning. All learning is performed with skin inputs. *Note*: Full connectivity implies that the network has all the excitatory connections intact. The grey zone indicates the range of cross-correlation measures obtained with the Full connectivity. (**C**) The impact of removing specific types of outgoing inhibitory neuron synaptic connections on the learning. *Note*: Full connectivity implies that the network has all inhibitory connections. (**D, E**) Similar to **B, C**, where learning is performed with Gaussian inputs. The excitatory and inhibitory synaptic connections between ENs and INs were labelled as, "***EE***": connections between excitatory - excitatory neurons, "***EI***": connections between excitatory - inhibitory neurons, "***II***": connections between inhibitory - inhibitory neurons, "***IE***": connections between inhibitory - excitatory neurons. The topological connectivity between ENs and INs were labelled as, "***Lat***": Lateral connections withing the ENs and INs in given layers, "***FF***": feed-forward connections from ENs and INs in layer 1 to layer 2, "***FB***": feed-back connections from ENs and INs in layer 2 to layer 1. (*insert*) "***Loc***": Local connections between neighboring ENs and INs (local connection between EN_i and IN_i). The network has initial connectivity of 37% (log-normal distribution, μ = 0.5, σ_{cv} = 10%, Fig. 8, 9). Ten different randomized initial weight vectors were generated for the same distribution parameters (individual marker for each given network configuration in **B-E**). All the network configuration learn with an excitatory synaptic filter of $e^{1.4}$(Fig. 4A, dotted line).